

WHAT SETS THE RADIAL LOCATIONS OF WARM DEBRIS DISKS?

NICHOLAS P. BALLERING, GEORGE H. RIEKE, KATE Y. L. SU, ANDRÁS GÁSPÁR
Steward Observatory, University of Arizona, 933 North Cherry Avenue, Tucson, AZ 85721, USA

ABSTRACT

The architectures of debris disks encode the history of planet formation in these systems. Studies of debris disks via their spectral energy distributions (SEDs) have found infrared excesses arising from cold dust, warm dust, or a combination of the two. The cold outer belts of many systems have been imaged, facilitating their study in great detail. Far less is known about the warm components, including the origin of the dust. The regularity of the disk temperatures indicates an underlying structure that may be linked to the water snow line. If the dust is generated from collisions in an exo-asteroid belt, the dust will likely trace the location of the water snow line in the primordial protoplanetary disk where planetesimal growth was enhanced. If instead the warm dust arises from the inward transport from a reservoir of icy material farther out in the system, the dust location is expected to be set by the current snow line. We analyze the SEDs of a large sample of debris disks with warm components. We find that warm components in single-component systems (those without detectable cold components) follow the primordial snow line rather than the current snow line, so they likely arise from exo-asteroid belts. While the locations of many warm components in two-component systems are also consistent with the primordial snow line, there is more diversity among these systems, suggesting additional effects play a role.

Keywords: circumstellar matter – planetary systems

1. INTRODUCTION

A debris disk comprises a remnant population of planetesimals on circumstellar orbits and the dust generated by their collisional destruction. While observations of protoplanetary disks show planetary systems in the early stages of formation, debris disks reveal the properties of more mature systems. The spatial structure of a debris disk traces the architecture of the planetary system because planets remove planetesimals from their vicinity. The interpretation of debris disk observations involves connecting the properties of the dust to those of the unseen planetesimals and planets. For recent reviews of debris disk science, see [Wyatt \(2008\)](#) and [Matthews et al. \(2014b\)](#).

Hundreds of spatially unresolved debris disks have been characterized by the infrared excess observed in the SEDs of their systems—the thermal emission of the debris disk dust. This excess can often be modeled simply with one or two blackbody functions, and it typically takes the form of a cold component (<130 K), a warm component (~ 190 K), or both ([Morales et al. 2011](#); [Ballering et al. 2013](#); [Chen et al. 2014](#)).¹ [Kennedy & Wyatt \(2014\)](#) concluded that for most systems the warm and cold components arise from radially distinct distributions of dust (as opposed to being co-located and having different temperatures due to different grain properties).

The cold components are the best-studied parts of debris disk systems. They reside far enough (i.e. $>$ tens of au) from their host stars that some have been resolved, revealing a belt analogous to the Kuiper belt in the solar system. The nature of the warm components is less certain, as they reside closer to the star and cannot easily be spatially resolved. For example, the nearby (7.7 pc) star Fomalhaut hosts a well-studied cold belt that has been resolved at several wavelengths ([Kalas et al. 2005](#); [Acke et al. 2012](#); [Boley et al. 2012](#); [MacGregor et al. 2017](#)). From analyses of its SED and infrared images, Fomalhaut also hosts a warm component ([Stapelfeldt](#)

[Ballering et al. 2013](#); [Chen et al. 2014](#)).¹ [Kennedy & Wyatt \(2014\)](#) concluded that for most systems the warm and cold components arise from radially distinct distributions of dust (as opposed to being co-located and having different temperatures due to different grain properties).

¹ [Su & Rieke \(2014\)](#) identified five dust components that a debris disk can possess, which, in addition to the warm and cold components described here, also include: a blowout halo of small grains outside of the cold belt ([Augereau et al. 2001](#); [Su et al. 2005](#)); exozodiacal dust that is hotter and nearer to the star than the warm dust and emits at ~ 10 μm ([Kennedy & Wyatt 2013](#); [Ballering et al. 2014](#)); and very hot dust emitting in the near-IR ([Absil et al. 2013](#); [Ertel et al. 2014](#)) likely composed of nanograins trapped in the stellar magnetic field ([Rieke et al. 2016](#)).

et al. 2004; Su et al. 2013), but obtaining resolved images of this warm component to confirm its properties remains difficult (Su et al. 2016). In this study, we draw conclusions about warm components by analyzing the SEDs of a large sample of sources and examining how their properties vary with the properties of their host stars.

The origin of the warm dust is heavily debated in the literature. Given that these components originate from zones likely well-populated by planets, one might expect the belts to be so strongly disturbed that all traces of their origins are erased. However, Morales et al. (2011) found a similarity in the warm belt temperatures among stars of different masses², suggesting a common underlying structure, possibly related to the water snow line. There are two general hypotheses regarding the source of such structures: (1) the dust is produced in-situ by the collisional processing of a belt of parent bodies analogous to the asteroid belt in the solar system, or (2) the dust is transported inward from an outer reservoir of cold planetesimals. As we will describe later, both of these possibilities predict that the locations of warm components will be set by the snow line (i.e. where water ice condensation/sublimation occurs). However, these hypotheses differ as to whether it is the *primordial* snow line or the *current* snow line that sets the warm dust location. These two snow lines predict different relations between the location of the warm dust and the mass of the host star. By examining the observed trend between warm dust location and stellar mass (M_\star), we can determine which snow line (primordial or current) was responsible for setting the dust location, and thus which hypothesis for the origin of the dust is favored.

1.1. Hypothesis 1: In-situ Production and the Primordial Snow Line

If the warm dust is produced in-situ from an exo-asteroid belt, it is expected to occur near the primordial snow line. Several mechanisms predict an enhancement of solid material and planetesimal formation at (or near) the snow line in a protoplanetary disk. Water vapor diffusing outward through the disk will condense at the snow line and increase the density of solid material there (Stevenson & Lunine 1988). Icy, roughly meter-size bodies from the outer disk will migrate inward due to gas drag and will sublimate at the snow line, creating an enhancement of vapor and solids (Cuzzi & Zahnle

2004). The increase in the dust-to-gas ratio at the snow line can create a region of lower turbulence in the disk. This leads to lower collisional velocities, promoting planetesimal growth, and creates a gas pressure maximum that traps inward migrating solids (Kretke & Lin 2007; Brauer et al. 2008). The resulting population of planetesimals may become the parent bodies in the debris disk, or this may trigger the formation of a giant planet that will stir the planetesimals around it and prevent them from coalescing into a planet. The continued stirring will cause planetesimal collisions that yield warm dust for an extended period of time. This is similar to how the gravitational influence of Jupiter stirs the asteroid belt in the solar system (e.g. Petit et al. 2001). In any case, the location of the resulting warm dust is linked to the primordial snow line.

The temperature in the midplane of a protoplanetary disk is set primarily by viscous heating. Min et al. (2011) give the following relation for the location of the primordial snow line:

$$r_{\text{SL}} \propto M_\star^{1/3} \dot{M}^{4/9} \kappa_R^{2/9} f^{-2/9} \alpha^{-2/9} T_{\text{ice}}^{-10/9}, \quad (1)$$

where \dot{M} is the mass accretion rate, κ_R is the Rosseland mean opacity, f is the gas-to-dust ratio, α is the turbulent mixing strength, and T_{ice} is the ice sublimation temperature. Of these parameters, only \dot{M} is believed to vary significantly with stellar mass and thus is relevant for estimating the form of the $r_{\text{SL}}-M_\star$ relation. The mass accretion rate has been found to vary with stellar mass as $\dot{M} \propto M_\star^2$ over a large range of stellar masses, including the masses of the stars in our sample (Calvet et al. 2004; Muzerolle et al. 2005; Natta et al. 2006). This implies that $r_{\text{SL}} \propto M_\star^{1.2}$. As we will emphasize later, this relation is shallower than that for the current snow line. Other investigations into the location of the primordial snow line also predict the $r_{\text{SL}}-M_\star$ relation to be significantly shallower than the current snow line relation (Kennedy & Kenyon 2008; Martin & Livio 2013a).

1.2. Hypothesis 2: Inward Transport and the Current Snow Line

If, instead, the warm dust is transported inward from an outer reservoir during the present debris disk phase, it is expected to reside at the current snow line. There are two plausible mechanisms for the inward transport. The first mechanism is analogous to that described by Nesvorný et al. (2010), who found that most of the warm dust in the inner region of the solar system originates from the disruption of Jupiter family comets (JFCs). JFCs are dynamically controlled by Jupiter and have orbits with significantly lower eccentricities and smaller aphelia than Halley-type comets or long-period comets. Simulations show that JFCs likely origi-

² Kennedy & Wyatt (2014), on the other hand, found that for stars with effective temperatures greater than ~ 8500 K there are also a number of notably warmer disks (see their Figure 6). Nevertheless, in this paper we analyze the locations of the dust belts, rather than their temperatures (which depend both on the dust location and grain sizes.)

inate in the Kuiper belt and are dynamically passed inward by the giant planets (Levison & Duncan 1997), with some JFCs arriving on asteroid-like orbits inside that of Jupiter (Rickman et al. 2017). When JFC orbits cross the current snow line, they begin to sublimate and eventually disintegrate, releasing dust. Simulations of generic planetary systems also show that a chain of several planets is required to efficiently transport planetesimals inward from an outer reservoir (Bonsor et al. 2012, 2014). This is consistent with the idea that the region between the snow line and the cold belt is maintained by one or more planets (Su et al. 2013).

For the second mechanism, dust generated by collisions in the outer parent body belt flows inward due to Poynting-Robertson (P-R) drag and stellar wind drag. While Wyatt (2005) argued that most disks we can detect are collision-dominated rather than drag-dominated (that is, grains are destroyed by mutual collisions faster than they can move inward), Kennedy & Piette (2015) noted that some inward transport is inevitable unless planets are present interior to the cold belt to remove the inflowing dust. Since these grains originate in the outer part of the system, they may contain a mixture of icy and refractory material. When the grains reach the snow line, the ices sublimate, reducing the grain size and consequently increasing the ratio of the radiation force to the gravitational force on the grain (β). This halts the grain’s inward motion and eventually causes it to be expelled outward. The net result is a pile-up of grains at the location of the current snow line (Kobayashi et al. 2008). However, numerical simulations (van Lieshout et al. 2014) indicate that the inward flow via this mechanism may be inadequate to maintain the amount of warm dust required for detectable infrared excesses with *Spitzer*, even with the snow line pile-up.

The location of the current snow line is determined by the incident stellar flux, so it scales as $r_{\text{SL}} \propto L_{\star}^{1/2}$, where L_{\star} is the stellar luminosity. Combining this with $L_{\star} \propto M_{\star}^4$, the typical relation between stellar luminosity and mass, yields $r_{\text{SL}} \propto M_{\star}^2$. Importantly, the current snow line relation is steeper than the primordial snow line relation (index of 2.0 versus 1.2).

1.3. Overview

In this paper, we analyze the SEDs of a sample of debris disks with warm components and infer the stellocentric locations of the warm dust. The dust location derived solely from an SED is subject to many uncertainties and cannot be determined absolutely for any given system. Therefore we focus our attention on the relative behavior of dust location with stellar mass, while holding all other parameters (e.g., grain materials) constant—except for the minimum grain size, which is known to vary systematically with stellar properties.

We examine the $r_{\text{dust}}-M_{\star}$ trend and compare the slope with those predicted by the primordial and current snow lines, providing insight into which snow line sets the dust location. From this we can deduce the the origin of the warm dust components.

2. METHODS

2.1. Target Selection

For our sample, we used the systems with a warm component found by Ballering et al. (2013), where “warm” was defined as warmer than 130 K. All of these systems have data available from the Multiband Imaging Photometer for *Spitzer* (MIPS; Rieke et al. 2004) at 24 and 70 μm and from the *Spitzer* Infrared Spectrograph (IRS; Houck et al. 2004).

Throughout the analysis, we separated the systems with only a warm component from those that also possess a detected cold component. The systems without a detected cold component should provide less ambiguous results, since these warm components could not arise from particles moving inward from cold belts via P-R drag, although they could still arise from comets originating in cold components that are below the current detection limit (Wyatt et al. 2007). In addition, modeling systems with a single dust component is less complicated and the results have less uncertainty.

Ballering et al. (2014) discovered silicate emission features in the IRS spectra of 22 of these systems. These features revealed the presence of exozodiacal dust, which is believed to reside at a different location than the typical warm component. Ballering et al. (2014) found that, besides the exozodiacal dust, an additional colder component was also required to fit the full IRS spectra of these sources. Whether this remaining excess consists of one or multiple components is difficult to determine. Thus, to ensure a pure sample of warm components, we excluded these 22 targets. If, however, the dust components giving rise to these features are a natural extension of standard warm components, then excluding these targets may introduce a bias to our sample.

We also excluded HIP 32435 (HD 53842) because the IRS data may have been contaminated by background sources (Donaldson et al. 2012). We removed additional targets in the course of our fitting procedure, as described in Section 2.6. The remaining 83 targets used for our analysis are listed in Table 1.

2.2. Stellar Properties

The stellar temperature (T_{\star}), luminosity, and distance from Earth (d) of most of our targets were taken from McDonald et al. (2012), who derived T_{\star} and L_{\star} by fitting the visible and near-IR photometry of these systems with stellar SED models. We then obtained the stellar

mass (M_*) from L_* using the (broken) power-law relation by Eker et al. (2015). McDonald et al. (2012) assumed a 10% uncertainty on the photometry they used to derive L_* , so we also assumed a 10% uncertainty on L_* . Combining this with the intrinsic 25–38% scatter in the L_* values Eker et al. (2015) used to derive their relations yields a \sim 6–10% uncertainty on our M_* values. For the targets not listed in McDonald et al. (2012, denoted with an “a” after the target name in Table 1), we inferred their stellar properties from their $V - K$ color using the tabulated values maintained online³ by E. Mamajek as an expanded and updated version of Table 5 in Pecaut & Mamajek (2013).

We required a model spectrum of the stellar photosphere for each of our targets, both for modeling the photospheric contribution to the observed SED and for calculating the temperature of dust grains when generating model spectra of the dust emission. We used an ATLAS9 (Castelli & Kurucz 2004) photosphere model with $\log g = 4.0$, solar metallicity, and T_* closest to that for each target (at most a difference of 125 K). These photosphere model spectra were modeled only out to 160 μm , so for completeness we extended them to 10,000 μm by extrapolating with a Rayleigh-Jeans power-law. We normalized the integrated spectra to L_* for each target. (Although during the fitting process we allowed the amplitude of the model photosphere to vary by a small amount to improve agreement with the photometry; see Section 2.6.)

2.3. IRS Data

While many infrared excesses have been identified from photometric measurements alone (Rieke et al. 2005; Su et al. 2006; Wyatt 2008; Matthews et al. 2014b; Sierchio et al. 2014), accurately measuring the temperature/location of the emitting dust requires the wide spectral coverage offered by IRS.

We obtained low-resolution IRS spectra for our targets from the LR7 release of The Combined Atlas of Sources with *Spitzer* IRS Spectra⁴ (CASSIS; Lebouteiller et al. 2011). Both long-low orders (LL1: 19.5–38.0 μm ; LL2: 14.0–21.3 μm) were available for all targets, and one or both of the short-low orders (SL1: 7.4–14.5 μm ; SL2: 5.2–7.7 μm) were also available for most of the targets. The IRS Astronomical Observation Requests numbers (AORs) for our targets are given in Table 1.

We removed outlying points more than 3σ away from a third-degree polynomial fit to the measurements in

each spectral order. To remove offsets between orders, we multiplied the LL1, SL1, and SL2 flux density values by correction factors (determined by eye), to align them with the LL2 order and to each other. The choice to pin the other orders to LL2 was arbitrary but had no effect on the results because, as described in Section 2.6, the amplitude of the whole IRS spectrum was varied as part of the fitting process. These correction factors (designated x_{LL1} , x_{SL1} , and x_{SL2}) are listed in Table 1. During this process we opted to remove HIP 79631 from our sample because the offsets between the orders were much greater than for any other target, suggesting the data may be unreliable.

2.4. IR and Sub-mm Photometry

In addition to the IRS data, we included in our SEDs photometry from MIPS at 24 and 70 μm plus additional photometry at wavelengths ≥ 70 μm from the literature. These data are listed in Table 2. Upper limits are at the 3σ level.

2.5. Modeling Dust Emission

Careful restriction of the model characteristics was necessary to avoid degeneracies that would undermine our ability to determine the trend of warm dust location with stellar mass. We assumed that the dust lies in a circular ring. To test the sensitivity of our conclusions to the particular ring geometry we used two different models: one with a constant ring width (independent of radius) and a second with a ring width that was a constant fraction of the ring radius. We discuss the first set of models here and the second set in Section 4.1 where we explore the robustness of our results. For these models, we assumed that the ring has $r_{\text{out}} = r_{\text{in}} + 2$ au (r is the stellocentric distance). We modeled the surface number density of grains as $\Sigma(r) \propto r^{-p}$ with $p = 1$, but varying this parameter within reasonable bounds had virtually no effect on our results. We assumed a power-law grain size distribution ($n(a) \propto a^{-q}$ where a is the grain radius) with size index $q = 3.65$ (Gáspár et al. 2012), minimum grain size $a_{\text{min}} = a_{\text{BOS}}$ (a_{BOS} is the blowout size), and maximum grain size $a_{\text{max}} = 1000$ μm . Grains larger than a_{max} contribute negligibly to the overall emission. We assumed a grain composition of 60% astronomical silicates and 40% organic refractory material by volume (Ballering et al. 2016). To test how robust our conclusions are to grain composition, we report on similar models with grains composed entirely of astronomical silicates in Section 4.1. The only free parameters in our dust belt models were r_{in} and the total mass of dust.

Fixing the minimum grain size to the predicted blowout size was an important step in the modeling because a_{BOS} varies systematically with stellar type and

³ http://www.pas.rochester.edu/~emamajek/EEM_dwarf_UBVIJHK_colors_Teff.txt

⁴ The Combined Atlas of Sources with *Spitzer* IRS Spectra (CASSIS) is a product of the IRS instrument team, supported by NASA and JPL. <http://cassis.sirtf.com/>

a_{\min} can have a substantial effect on the derived dust location (a smaller value of a_{\min} leads to a larger inferred r_{in}). That is, we do not simply link the dust temperature and location using the blackbody temperature. The choice to use $a_{\min} = a_{\text{BOS}}$ is justified theoretically and also empirically. Detailed fits to debris disk spectra exhibiting silicate emission features were able to constrain both the dust location and minimum grain size; these fits showed the minimum spherical grain size to be consistent with the blowout size (Ballering et al. 2014). Furthermore, Booth et al. (2013) compared the sizes of cold debris disks, as measured from their resolved *Herschel* images and as derived from fitting blackbody functions to their SEDs, and found that the differences could be largely explained by models assuming $a_{\min} = a_{\text{BOS}}$, although in a similar analysis Pawellek et al. (2014) found a_{\min} values somewhat larger than a_{BOS} .

The blowout size is the largest grain size for which $\beta > 0.5$, where β is the ratio of the radiation force to the gravitational force on a grain. For spherical grains, β is given by

$$\beta = \frac{3L_{\star}}{16\pi GM_{\star}ac\rho} \frac{\int_0^{\infty} Q_{\text{pr}}(\lambda, a)F_{\lambda\star}(\lambda) d\lambda}{\int_0^{\infty} F_{\lambda\star}(\lambda) d\lambda}, \quad (2)$$

where $F_{\lambda\star}(\lambda)$ is the stellar flux density, $Q_{\text{pr}}(\lambda, a)$ is the radiation pressure efficiency on the grain, G is the gravitational constant, c is the speed of light, and $\rho = 2.34 \text{ g cm}^{-3}$ is the grain density (2.7 g cm^{-3} for the astronomical silicates and 1.8 g cm^{-3} for the organic refractory material). We computed $Q_{\text{pr}}(\lambda, a)$ and the absorption efficiency, $Q_{\text{abs}}(\lambda, a)$ (needed to model the dust emission as discussed later) from the optical constants using the Mie theory code `miex` (Wolf & Voshchinnikov 2004). The optical constants of this grain composition mixture are given in Table 3 of Ballering et al. (2016). a_{BOS} for each target is given in Table 1.

To compute the model dust emission, we needed the temperature of the grains (T_{dust}) as a function of their radial location and size. We calculated this by computing

$$r(T_{\text{dust}}, a) = \frac{1}{4\pi} \sqrt{\frac{\int Q_{\text{abs}}(\lambda, a)L_{\lambda\star}(\lambda) d\lambda}{\int Q_{\text{abs}}(\lambda, a)B_{\lambda}(\lambda, T_{\text{dust}}) d\lambda}} \quad (3)$$

then inverting it to solve for $T_{\text{dust}}(r, a)$. $L_{\lambda\star}(\lambda)$ is the stellar spectral luminosity, and $B_{\lambda}(\lambda, T_{\text{dust}})$ is the Planck function. Equation 3 is derived from balancing the heating and cooling power on the grain. Finally, we calculated the emission spectrum from each grain,

$$F_{\nu}(\lambda, r, a) = \left(\frac{a}{d}\right)^2 Q_{\text{abs}}(\lambda, a)\pi B_{\nu}(\lambda, T_{\text{dust}}), \quad (4)$$

and combined these spectra into a single spectrum weighted by the spatial distribution and grain size distribution of the model.

2.6. Fitting Models to the Observed SEDs

We fit the observed SED of each target, including photometric points at V , J , H , and K , the IRS spectrum, and the additional photometry listed in Table 2. The stellar photosphere accounts for virtually all of the observed flux density in the visible and near-IR, but it also contributes significantly at longer wavelengths. We modeled the photospheric contribution to the SED as described in Section 2.1, and we allowed small adjustments in the photospheric level to optimize the fits. To fit the excess emission from the debris disk, we used three different models: (1) a single modified blackbody (described later), which we used to double-check for systems that could be fit best by a single cold component; (2) a single warm dust belt, as described in Section 2.5, with the location of the dust ($r_{\text{warm}} = r_{\text{in}}$) and the mass of dust in the belt (M_{warm}) as free parameters; and (3) a warm dust belt plus a modified blackbody, with the blackbody accounting for a possible cold component. We did not fit the cold components with our dust belt model because their locations were not of interest for our analysis.

For the modified blackbody, we followed the formulation used by Kennedy & Wyatt (2014):

$$F_{\nu}(\lambda) = c_{\text{BB}}B_{\nu}(\lambda, T_{\text{cold}})X(\lambda)^{-1}, \quad (5)$$

where c_{BB} is a constant (amplitude), T_{cold} is the temperature of the cold component, and

$$X(\lambda) = \begin{cases} 1 & \lambda < \lambda_0 \\ (\lambda/\lambda_0)^{\tilde{\beta}} & \lambda > \lambda_0 \end{cases}. \quad (6)$$

The modification to the blackbody, $X(\lambda)$, models the steeper than Rayleigh-Jeans fall off at long wavelengths due to grains not emitting efficiently at wavelengths longer than their size. The free parameters for the modified blackbody were c_{BB} , T_{cold} , λ_0 , and $\tilde{\beta}$. In the fitting we required $50 \mu\text{m} < \lambda_0 < 500 \mu\text{m}$, $0 < \tilde{\beta} < 2$, and $T_{\text{cold}} < 130 \text{ K}$ when part of a two-component fit.

In the fitting process, we also allowed for a small amplitude adjustment to the IRS data (c_{IRS}), which we allowed to take values between 0.8 and 1.2. This effectively corrected any systematic calibration error. This procedure yielded good results with c_{IRS} constrained at two points: first, the short end of the IRS data needed to match the photosphere model, which in turn had to match the visible/near-IR photometry; second, the IRS data needed to match the MIPS photometry point at $24 \mu\text{m}$ in order for the best fit model to pass through both the MIPS and IRS data at this wavelength.

In practice, we performed a grid search over r_{in} (in steps of 0.1 au) and c_{IRS} (in steps of 0.01). At each point in the grid we then found best values for the rest of the free parameters with a Levenberg-Marquardt al-

gorithm (the Matlab function `lsqcurvefit`). The best fit was the model that minimized the standard χ^2 metric. When calculating χ^2 , we enhanced the weights of the photometry points at $\geq 70 \mu\text{m}$ by a factor of 25 to balance their influence on the fit against the large number of points in the IRS spectra. Without this extra weighting, the behavior of the model in the far-IR/sub-mm often reflected an extrapolation from the longest wavelength IRS points, rather than fitting to the data in this wavelength regime. Upper limit photometry measurements were not included in the χ^2 calculation, but we inspected the best-fitting models to ensure they were consistent with these measurements. Parameters λ_0 and β were often not well-constrained by the fitting, except for the targets with accurately measured far-IR/sub-mm photometry.

We inspected the results of our single blackbody fits to ensure that we only included genuine warm components in our sample. Targets that were fit well by a single blackbody with temperature < 130 K were discarded from our sample. These included HIPs 544, 2072, 9141, 16852, 17764, 24947, 46843, 51194, 59072, 59960, 61960, 65728, 66065, 90936, and 107649. Some of these targets had single warm components with temperatures just above the 130 K cutoff according to Ballering et al. (2013), but with the additional far-IR photometry and the new fitting procedure used here, they now fell below this cutoff. For others, Ballering et al. (2013) had found two components with the warm component being relatively weak, but here we found that the warm component was no longer necessary to fit the IRS data.

We also excluded HIP 6276 because it has an extremely weak warm excess (and no evidence for a cold component) from which we could not place any meaningful constraints on the dust location. Finally, we excluded HIP 53954 and HIP 65109, because any model fit to the IRS data significantly over-predicted the far-IR photometry. A similar steep decline of the disk flux in the far-IR has been noted in a few other disks (Ertel et al. 2012), requiring a very unusual distribution of grain sizes to model.

We examined the fits of the remaining targets to determine which were best fit with a single warm belt and which required a cold component as well. In many cases, the requirement for a cold component came from the far-IR photometry, with the IRS data fitting well with a single warm belt. We included a cold component when the warm-only model under-predicted the far-IR data by more than 2σ (with the offset from multiple far-IR points combined in quadrature) and the addition of a cold component improved the fit. For most systems, the designations agreed with those of Ballering et al. (2013). Five systems that previously had been fit with a single warm component now were fit with two com-

ponents (HIPs 1473, 1481, 77432, 78045, and 85922), and two systems that previously had been fit with two components were now fit best with a single warm belt (HIP 63836 and HIP 112542). The best fit cold component of HIP 117452 had $T_{\text{cold}} = 130$ K (the upper bound allowed by the fit), suggesting this system has an unusually warm cold component. However, the model fit the data well, so a significantly higher value of T_{cold} is likely not required. An unusually warm cold component does not, however, impact the need for a separate warm belt, as we found that a single component could not fit all the data.

From our χ^2 metric, we found that the median statistical uncertainties on r_{in} were 5% and 13% for the single-component and two-component systems, respectively. We calculated the luminosities of the best fit model components by integrating under the model spectra. We then derived the fractional luminosity of each component: $f_{\text{warm}} = L_{\text{warm}}/L_{\star}$ and $f_{\text{cold}} = L_{\text{cold}}/L_{\star}$. The results of the fitting are given in Tables 3 and 4. The best fit model SED for each target is shown in Figures 7 and 8. Our final sample had 29 systems with single warm components and 54 systems with two components.

3. ANALYSIS AND RESULTS

With the locations of the warm dust components for our targets found, we next turned our attention to the relationship between the dust location and the stellar mass. We expected the relation to follow a power-law ($r_{\text{warm}} \propto M_{\star}^b$), considering the predicted relations for both the primordial and current snow lines take this form. Our goal was to measure the value of the exponent b and see if it aligned with the predicted value for the current or primordial snow line. We did not attempt to compare the absolute values of the measured dust locations to those predicted for the snow lines. The actual location of the primordial snow line is less certain than its predicted relation with stellar mass, considering the uncertainty on the values of all the factors in Equation 1 and the fact that the primordial snow line location likely evolves with time. Nevertheless, Martin & Livio (2013b) did find that the absolute stellocentric distances of warm debris disks reported in the literature were roughly consistent with the location of the primordial snow line.

3.1. Single-component Systems

We first considered the systems with a single warm component. Figure 1 plots r_{warm} versus M_{\star} and shows clear evidence for a positive trend. To quantify this trend, we fit the function $\log(r_{\text{warm}}/\text{au}) = a + b \log(M_{\star}/M_{\odot})$ to these points. The best fit values of

b and a were computed as

$$b = \frac{\overline{\log(M_\star) \cdot \log(r_{\text{warm}})} - \overline{\log(M_\star)} \cdot \overline{\log(r_{\text{warm}})}}{\overline{\log(M_\star)^2} - \overline{\log(M_\star)}^2} \quad (7)$$

and $a = \overline{\log(r_{\text{warm}})} - b \cdot \overline{\log(M_\star)}$. We found $b = 1.08$, $a = 0.566$ (i.e. $r_{\text{warm}}/\text{au} = 3.68(M_\star/M_\odot)^{1.08}$). This best fit trend line is plotted with the data points in Figure 1.

Considering the substantial amount of scatter evident in the data around the trend line, we used a bootstrap procedure to quantify the significance of our derived value of b . We used 10,000 trials for the bootstrap procedure. For each trial we randomly selected 29 points (with replacement) from our sample and recomputed the best fit b using Equation 7. Figure 2 shows the distribution of b values found by the bootstrap procedure. The distribution was fit by a normal distribution with mean = 1.08 and $\sigma = 0.21$ using the Matlab function `fitdist`.

We found that b for the targets with a single warm component was consistent (within 0.6σ) with the value predicted by the primordial snow line (1.2) but was not consistent ($> 4.3\sigma$) with the relation predicted by the current snow line (2.0). Thus we conclude that these warm components are more likely to arise from dust produced by exo-asteroid belts than from disintegrating comets or dust dragged inward from an outer belt that is below our current detection limit.

3.2. Two-component Systems

Next we examined the $r_{\text{warm}}-M_\star$ trend for the two-component systems, shown in Figure 3. There was more scatter than for the single-component systems, and no simple relation was evident that represented all the points. For comparison, we added to this plot the best fit trend found for the single-component systems (green dashed line from Figure 1). We found that many of the warm components in the two-component systems were consistent with this same trend, but there were also several systems both above and below the trend.

3.3. Scatter around the Single-component Trend

We subtracted the values of r_{warm} predicted by the trend line for the single-component systems from the measured r_{warm} values in both samples. Fitting a normal distribution to residuals of the single-component systems (using `fitdist`) gave a mean = 0.0 and $\sigma=0.16$ dex in $\log(r_{\text{warm}}/\text{au})$. This provided a measure of the inherent scatter around this trend for systems that likely follow the primordial snow line relation. The 1σ region around the trend due to this scatter is depicted in Figures 1 and 3 with thin dotted green lines.

Figure 4 shows the distribution of the residual warm dust locations from the trend (green for the single-component systems, magenta for the two-component

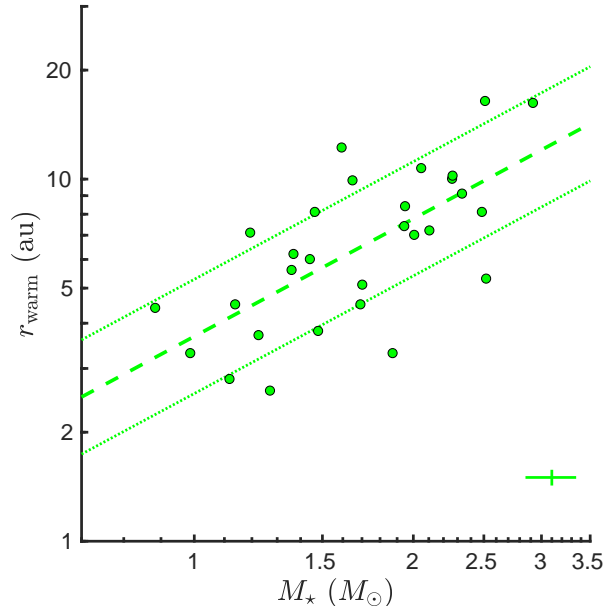


Figure 1. Location of the warm dust vs, stellar mass for the 29 targets with a single dust component. The dashed line shows the best fit trend $\log(r_{\text{warm}}/\text{au}) = 0.566 + 1.08 \log(M_\star/M_\odot)$, equivalent to $r_{\text{warm}}/\text{au} = 3.68(M_\star/M_\odot)^{1.08}$. The thin dotted green lines show the measured 1σ scatter around the trend (± 0.16 dex). A representative error bar is in the lower-right, showing the typical 8% uncertainty on M_\star and 5% uncertainty on r_{warm} .

systems). The distribution for the two-component systems peaks around the trend (no residual). We note that $32/54 = 59\%$ of these systems fall within the 2σ tolerance of the trend for the systems with only warm components. The histogram shows for the two-component systems a decreasing tail of warm dust locations below the trend (negative residual), whereas the warm dust locations above the trend show signs of a separate population of systems. It may be that some warm components in two-component systems have locations set by the primordial snow line while others end up off of this trend for various reasons. Alternatively, these warm components may have locations scattered more or less randomly, with some inevitably falling along the trend set by the single-component systems. In Section 4.2 we discuss various possibilities for the nature of the warm components in two-component systems.

4. DISCUSSION

4.1. Effect of Model Assumptions

An essential feature of our analysis is that we compare the trend of warm dust location with stellar mass to the predicted trend for the two possible snow lines. By comparing trends rather than absolute values, we expect that systematic errors due to our choice of model disk geometry or grain composition (optical constants) will

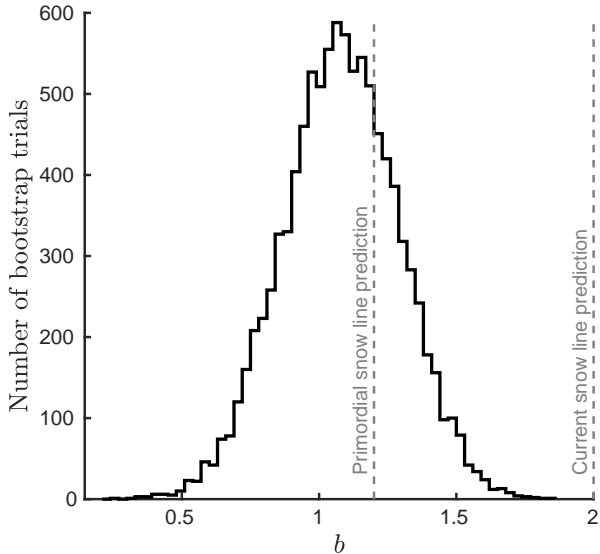


Figure 2. Distribution of the results from the bootstrap procedure to estimate the uncertainty on the power-law index (b) of the observed $r_{\text{warm}}-M_{\star}$ relation for systems with a single component. The distribution has mean = 1.08 and $\sigma = 0.21$. The warm components are thus consistent with being set by the primordial snow line and inconsistent with being set by the current snow line.

not influence our results. To test what role our model assumptions may have had on our results, we repeated our analysis twice with different assumptions. First, we re-fit the SEDs with dust belts with fractional widths of $0.4 r_{\text{in}}$ (in contrast to the fixed belt width of 2 au we used in the main analysis). The results agreed almost exactly with those of our main analysis: the single-component systems showed a clear trend in belt location with stellar mass while the two-component systems showed considerable scatter. A bootstrap analysis of the single-component power-law index yielded $b = 0.95 \pm 0.19$. Second, instead of using a mixture of astronomical silicates and refractory organic material for the dust composition, we used 100% astronomical silicates (a common first-order assumption in debris disk modeling). Again, we found very similar results to our main analysis with $b = 1.26 \pm 0.21$. The r_{warm} vs, M_{\star} trends for all three sets of model assumptions are plotted together in Figure 5. Thus neither of these modifications to our model assumptions affected our main conclusion that the locations of single-component systems are consistent with the primordial snow line and inconsistent with the current snow line.

4.2. Origin of Warm Dust in Two-component Systems

We have shown that warm dust in the single-component systems resides at locations consistent with being set by the primordial snow line and not by the current snow line, and thus is likely to originate from

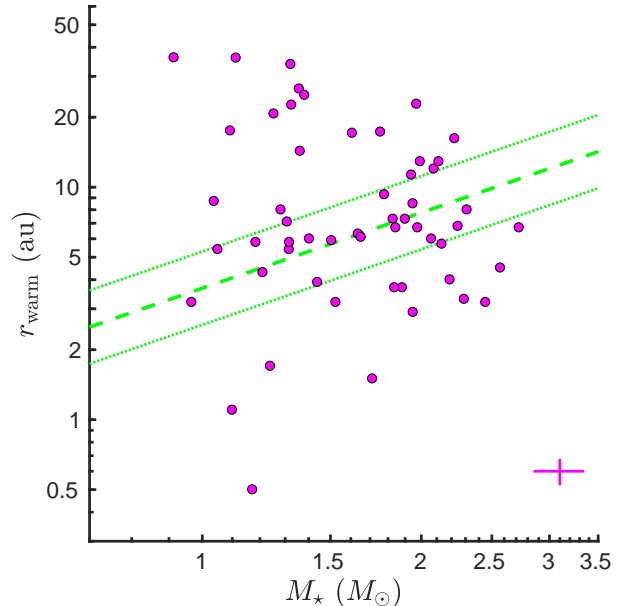


Figure 3. Location of the warm dust vs, stellar mass for the 54 targets with two dust components. The dashed green line is the best fit trend line derived for the single-component systems (as in Figure 1), which we found likely arise from asteroid belts with locations set by the primordial snow line. The thin dotted green lines show the measured 1σ scatter around the trend (± 0.16 dex). We see that many targets are consistent with this trend (suggesting they also are set by the primordial snow line) but there are also many sources located away from the trend. A representative error bar is in the lower-right, showing the typical 8% uncertainty on M_{\star} and 13% uncertainty on r_{warm} .

exo-asteroid belts. The warm dust locations in two-component systems are much more scattered, although many reside at similar locations to those in single-component systems. Here we turn our attention to the nature of the two-component systems, especially those with warm components that clearly do not trace the primordial snow line location.

4.2.1. Planets?

Planets are known to sculpt debris disks, and the gap between warm and cold components is often ascribed to the presence of planets. Thus the scatter in warm dust locations may simply reflect a diversity in the locations of planet formation or in their dynamical histories. The warm dust may arise from the in-situ collisional processing of a parent body belt, but its location may not be set by the primordial snow line. However, this scenario makes no clear prediction as to why more scatter would arise in systems with two components than in systems with only a warm component, unless systems without cold components also have fewer planets.

4.2.2. Inward Transport?

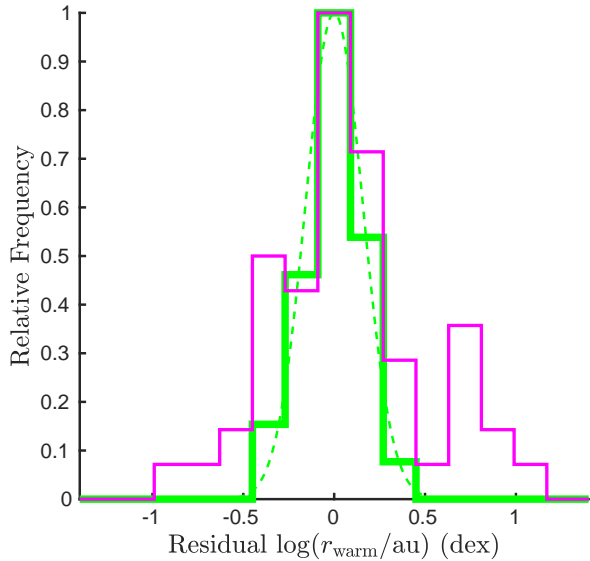


Figure 4. Distributions of the warm dust residual locations for the single-component (green) and two-component (magenta) systems around the trend line found for the single-component systems. The single-component systems show a symmetric distribution of residuals with mean = 0.0 and $\sigma = 0.16$ dex. A normal distribution with this mean and σ is shown in the dotted green line. All three curves are unity normalized in order to better compare their shapes. The two-component systems show a peak centered on the trend, a tail of systems below the trend, and a separate population of systems above the trend.

As discussed earlier, the inward transport of material from the cold outer belt is expected to result in warm dust at a preferential location—the current snow line. However, these warm components span a large range of locations for a given stellar mass, so it is unlikely that inward transport could explain all of these systems.

The specific scenario of inward transport by drag forces predicts that the warm component of dragged in material should be much fainter than the cold reservoir from which it originates (Kennedy & Piette 2015). We looked for this in our sample by plotting the fractional luminosities of the warm⁵ and cold components—and their ratio—against the residual warm dust location from the trend (Figure 6). We found that the $f_{\text{warm}}/f_{\text{cold}}$ ratio (bottom panel) is roughly the same across our entire sample (or perhaps somewhat larger in systems below the trend). Thus this provides no additional support for the drag scenario. In fact, Geiler & Krivov (2017) found that the $f_{\text{warm}}/f_{\text{cold}}$ ratios for two-component debris disks are consistent with the steady-

⁵ Note from the top panel of Figure 6 that the two-component systems (magenta points) near the trend have a similar brightness distribution as the single-component systems (green points), furthering the notion that these warm components arise from a common mechanism.

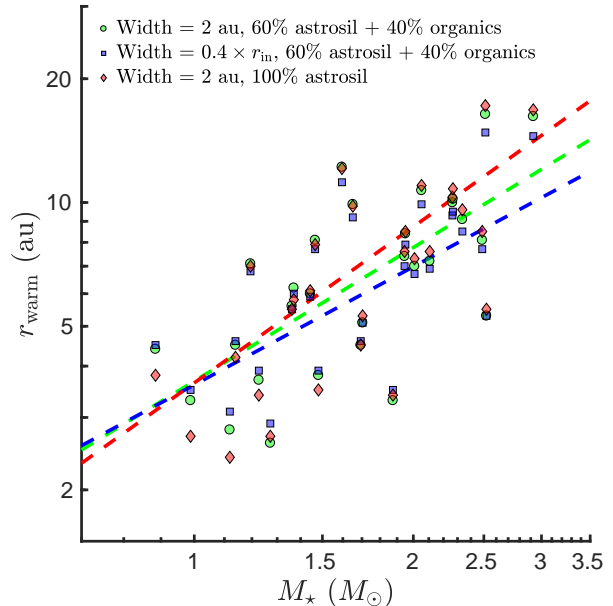


Figure 5. Warm dust location vs, stellar mass for the 29 single-component targets, with the warm dust location determined by three different models. The green circles assume the dust is located in a 2 au wide ring and is composed of a mixture of astronomical silicates and organic refractory material. These results were presented in Section 3 and are the same points shown in Figure 1. The blue squares assume the same dust composition, but use a ring width that scales as 0.4 times the ring’s location. The red diamonds again assume 2 au wide belts, but change the composition of the dust to pure astronomical silicates. The results are nearly identical for the three different sets of model assumptions. Therefore our conclusion that these warm belts are likely set by the primordial snow line and not by the current snow line is robust against our particular choice of model.

state collisional evolution of inner and outer parent body belts originating from protoplanetary disks with reasonable radial density profiles.

Later-type stars may be able to drag in a substantial amount of dust to generate a bright warm component if their luminosity is low enough such that no grains are blown out of the system by radiation pressure (there is no a_{BOS}). Drag is also enhanced in later-type stars by stronger stellar winds. With no significant radiation force on the grains, there would also be no pile-up of grains when the icy constituents sublime, so the warm components would not trace any snow line location. The systems in our sample, however, have sufficiently high luminosities that they should be able to blow grains out, so we deem this situation unlikely.

4.2.3. Contamination by Exozodiacal Dust?

The warm components that fall below the single-component trend line may result from exozodiacal dust components, which are considered a separate component from the traditional warm components (Su & Rieke

2014). We purposely discarded targets with exozodiacal dust from our sample (Section 2.1), so perhaps these systems should be ignored for the same reason. Two of the four systems with warm dust located more than 3σ below the trend (HIP 1481 and HIP 77432) show clear silicate features in their best fit model spectra, and silicate features are a signature of exozodiacal dust (Ballering et al. 2014). Ballering et al. (2014) found that all systems with exozodiacal dust also had outer components, consistent with finding such systems only in our two-component sample.

4.2.4. Contamination by Outer Dust?

For the systems with warm component locations above the trend, it is possible that we are not seeing dust interior to the cold component; rather, there is dust with a range of temperatures located within the outer belt. While Kennedy & Wyatt (2014) argued that this is not possible for most two-component systems, HIP 95270 (HD 181327), which we found to have r_{warm} above the trend, was an exception. In fact, Lebreton et al. (2012) fit the entire SED of this system with dust from a single outer belt.

It is also possible that we are seeing emission from the spatially unresolved blowout halo of small grains beyond the cold parent body belt. These grains must be small—potentially below the blowout size—so are warm despite their large stellocentric distance. From the middle panel of Figure 6 we see that the systems above the trend tend to have slightly higher than average cold component fractional luminosities, consistent with systems capable of generating large halos. Detailed studies of disks with such halos seen in resolved images have found that the halo component’s contribution to the SED often peaks at wavelengths shorter than the cold component but longer than a typical warm component (as is seen for the systems above the trend in our sample), although this varies among specific systems. For example, the halo of γ Ophiuchi peaks at nearly the same wavelength as the cold belt (Figure 3 of Su et al. 2008), the halo of HR 8799 peaks at a shorter wavelength (Figure 9 of Su et al. 2009), and the halo of β Pictoris peaks at an even shorter wavelength (Figure 14 of Ballering et al. 2016). In many systems with halos, the halo signal can simply blend with the cold belt in the SED and be fit as a single component. This may be especially true if there is also an inner warm component in the system. In fact, HR 8799 (HIP 114189) and γ Ophiuchi (HIP 87108)—which are known to have halos—are in our sample, but their halo components are not detected in our fitting separately from their cold components.

HIP 11847 (HD 15745), a system with a large r_{warm} value, has a fan-shaped outer component detected in scattered light images out to 450 au (Kalas et al. 2007;

Schneider et al. 2014), which may be a halo component, but no detailed models have shown that this halo could give rise to the warm part of the SED. Another such system, HIP 36948 (HD 61005 a.k.a. “The Moth”) is seen in scattered light to have an outer belt with wings of dust swept back due to interactions with the ISM (Hines et al. 2007; Buenzli et al. 2010; Schneider et al. 2014). Studies of this system’s SED that modeled the outer component with a modified blackbody (Kennedy & Wyatt 2010) or with a narrow belt (Ricarte et al. 2013) found the warm component to be fairly cold ($\sim 100\text{--}125\text{K}$)—consistent with the large value of r_{warm} found here (36.1 au). In contrast, Olofsson et al. (2016) modeled this SED with a wide outer belt plus a fainter and hotter ($\sim 220\text{K}$) warm component. This suggests the outer belt comprises grains with a range of temperatures, which our model accounts for with a warm component placed far from the star. This system demonstrates how cold components can add uncertainty to the derived locations of warm components.

4.2.5. Conclusion

We can identify no definitive source for the scatter in the warm dust locations of these two-component systems. Planets in a diversity of arrangements offer one explanation for this scatter. It may also be that the scatter arises from multiple mechanisms operating together, potentially including exo-asteroid belts (as is favored for the single-component systems), the presence of exozodiacal dust, contamination from warm dust in a halo or outer belt, and the inward transport of material by comets (although we deem inward transport by drag forces to be unlikely).

5. SUMMARY

1. Warm components of debris disks have been observed in the spatially unresolved SEDs of many stars, but the nature and origin of the dust is not known. There are two plausible hypotheses for its origin: the in-situ production of dust via collisions in an asteroid belt-like population of parent body planetesimals, or the inward transport of material from an outer reservoir.
2. The first hypothesis predicts the dust to be located at the primordial snow line, while the second hypothesis predicts the dust to be located at the current snow line. The location of the primordial snow line follows a shallower power-law relation with stellar mass than does the current snow line, providing a means to distinguish between the two.
3. We located the warm dust in 83 debris disk systems observed with *Spitzer*/IRS (29 with a single

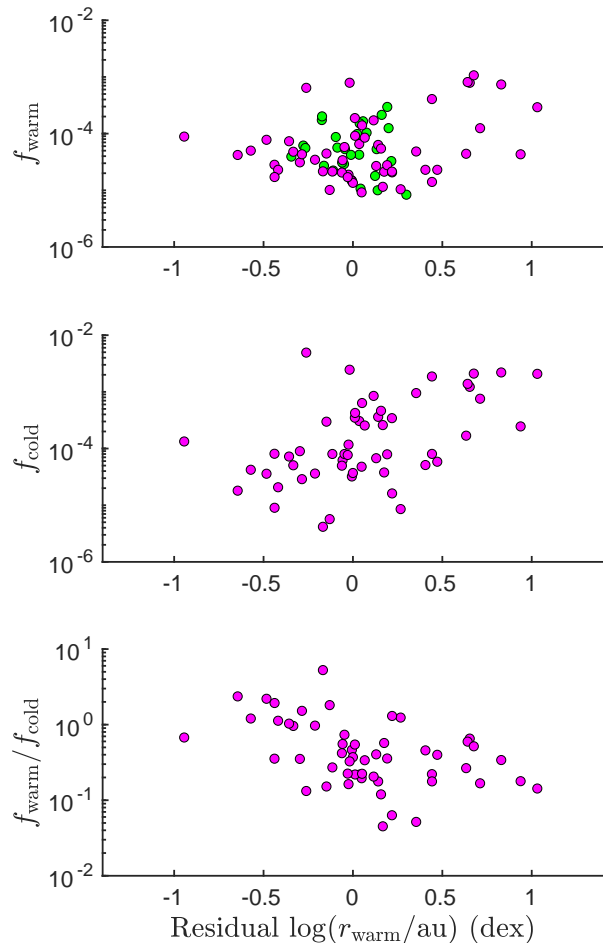


Figure 6. Fractional luminosity (brightness) of the warm components (top panel) and the cold components (middle panel), and the ratio of the two (bottom panel) vs. the residual warm dust locations relative to the best fit trend. The single-component systems are in green and the two-component systems are in magenta. The systems above the trend (on the right side of these plots) tend to have brighter than average warm and cold components, but the ratio of their brightnesses are in line with the sample as a whole.

warm component, 54 that also possess a cold component) by fitting model dust belt emission spectra to their SEDs.

4. We found that the $r_{\text{warm}}-M_{\star}$ trend for the single-component systems is consistent with the primordial snow line and not consistent with the current snow line. We thus favor the in-situ dust production scenario for these systems. Many of the two-component systems are also consistent with this relation. Hence we conclude that the collisional processing of exo-asteroid belts is a common mechanism to produce warm debris disk components.
5. We are not able to definitively explain the scatter of warm component locations in the two-component systems. Warm planetesimal belts with locations set by planets in a diversity of architectures offer a single mechanism to explain the scatter. Or the scatter could result from a mixture of systems with warm dust locations set by the primordial snow line and those set by other mechanisms. The inward transport of material by comets remains possible in these systems, and could contribute to the scatter. Warm belts nearer the star than the snow line may be exozodiacal dust, while those farther from the star may be warm dust collocated with the cold dust or even beyond the cold dust in a halo component.

We thank Glenn Schneider and the anonymous referee for many helpful comments on this paper. This work is based on observations made with the *Spitzer Space Telescope*, which is operated by the Jet Propulsion Laboratory, California Institute of Technology, under a contract with NASA.

Facility: *Spitzer* (IRS, MIPS).

Software: MATLAB, miex.

REFERENCES

- Abil, O., Defrère, D., Coudé du Foresto, V., et al. 2013, *A&A*, 555, A104
- Acke, B., Min, M., Dominik, C., et al. 2012, *A&A*, 540, A125
- Augereau, J. C., Nelson, R. P., Lagrange, A. M., Papaloizou, J. C. B., & Mouillet, D. 2001, *A&A*, 370, 447
- Ballering, N. P., Rieke, G. H., & Gáspár, A. 2014, *ApJ*, 793, 57
- Ballering, N. P., Rieke, G. H., Su, K. Y. L., & Montiel, E. 2013, *ApJ*, 775, 55
- Ballering, N. P., Su, K. Y. L., Rieke, G. H., & Gáspár, A. 2016, *ApJ*, 823, 108
- Boley, A. C., Payne, M. J., Corder, S., et al. 2012, *ApJL*, 750, L21
- Bonsor, A., Augereau, J.-C., & Thébault, P. 2012, *A&A*, 548, A104
- Bonsor, A., Raymond, S. N., Augereau, J.-C., & Ormel, C. W. 2014, *MNRAS*, 441, 2380
- Booth, M., Kennedy, G., Sibthorpe, B., et al. 2013, *MNRAS*, 428, 1263
- Booth, M., Jordán, A., Casassus, S., et al. 2016, *MNRAS*, 460, L10
- Brauer, F., Henning, T., & Dullemond, C. P. 2008, *A&A*, 487, L1
- Buenzli, E., Thalmann, C., Vigan, A., et al. 2010, *A&A*, 524, L1
- Calvet, N., Muzerolle, J., Briceño, C., et al. 2004, *AJ*, 128, 1294
- Carpenter, J. M., Wolf, S., Schreyer, K., Launhardt, R., & Henning, T. 2005, *AJ*, 129, 1049
- Castelli, F., & Kurucz, R. L. 2004, *ArXiv Astrophysics e-prints*, arXiv:astro-ph/0405087
- Chen, C. H., Mittal, T., Kuchner, M., et al. 2014, *ApJS*, 211, 25

- Corder, S., Carpenter, J. M., Sargent, A. I., et al. 2009, *ApJL*, 690, L65
- Cuzzi, J. N., & Zahnle, K. J. 2004, *ApJ*, 614, 490
- Donaldson, J. K., Lebreton, J., Roberge, A., Augereau, J.-C., & Krivov, A. V. 2013, *ApJ*, 772, 17
- Donaldson, J. K., Roberge, A., Chen, C. H., et al. 2012, *ApJ*, 753, 147
- Draper, Z. H., Matthews, B. C., Kennedy, G. M., et al. 2016a, *MNRAS*, 456, 459
- Draper, Z. H., Duchêne, G., Millar-Blanchaer, M. A., et al. 2016b, *ApJ*, 826, 147
- Eiroa, C., Marshall, J. P., Mora, A., et al. 2013, *A&A*, 555, A11
- Eker, Z., Soydogan, F., Soydogan, E., et al. 2015, *AJ*, 149, 131
- Ertel, S., Wolf, S., Marshall, J. P., et al. 2012, *A&A*, 541, A148
- Ertel, S., Absil, O., Defrère, D., et al. 2014, *A&A*, 570, A128
- Gáspár, A., Psaltis, D., Rieke, G. H., & Özel, F. 2012, *ApJ*, 754, 74
- Geiler, F., & Krivov, A. V. 2017, *MNRAS*, 468, 959
- Greaves, J. S., Hales, A. S., Mason, B. S., & Matthews, B. C. 2012, *MNRAS*, 423, L70
- Hillenbrand, L. A., Carpenter, J. M., Kim, J. S., et al. 2008, *ApJ*, 677, 630
- Hines, D. C., Schneider, G., Hollenbach, D., et al. 2007, *ApJL*, 671, L165
- Houck, J. R., Roellig, T. L., van Cleve, J., et al. 2004, *ApJS*, 154, 18
- Hughes, A. M., Wilner, D. J., Andrews, S. M., et al. 2011, *ApJ*, 740, 38
- Kalas, P., Duchene, G., Fitzgerald, M. P., & Graham, J. R. 2007, *ApJL*, 671, L161
- Kalas, P., Graham, J. R., & Clampin, M. 2005, *Nature*, 435, 1067
- Kennedy, G. M., & Kenyon, S. J. 2008, *ApJ*, 673, 502
- Kennedy, G. M., & Piette, A. 2015, *MNRAS*, 449, 2304
- Kennedy, G. M., & Wyatt, M. C. 2010, *MNRAS*, 405, 1253
- . 2013, *MNRAS*, 433, 2334
- . 2014, *MNRAS*, 444, 3164
- Kobayashi, H., Watanabe, S.-i., Kimura, H., & Yamamoto, T. 2008, *Icarus*, 195, 871
- Kretke, K. A., & Lin, D. N. C. 2007, *ApJL*, 664, L55
- Lebouteiller, V., Barry, D. J., Spoon, H. W. W., et al. 2011, *ApJS*, 196, 8
- Lebreton, J., Augereau, J.-C., Thi, W.-F., et al. 2012, *A&A*, 539, A17
- Levison, H. F., & Duncan, M. J. 1997, *Icarus*, 127, 13
- Lieman-Sifry, J., Hughes, A. M., Carpenter, J. M., et al. 2016, *ApJ*, 828, 25
- Liseau, R., Risacher, C., Brandeker, A., et al. 2008, *A&A*, 480, L47
- MacGregor, M. A., Wilner, D. J., Andrews, S. M., & Hughes, A. M. 2015, *ApJ*, 801, 59
- MacGregor, M. A., Wilner, D. J., Chandler, C., et al. 2016, *ApJ*, 823, 79
- MacGregor, M. A., Matra, L., Kalas, P., et al. 2017, *ArXiv e-prints*, arXiv:1705.05867
- Maness, H. L., Fitzgerald, M. P., Paladini, R., et al. 2008, *ApJL*, 686, L25
- Marino, S., Matrà, L., Stark, C., et al. 2016, *MNRAS*, 460, 2933
- Martin, R. G., & Livio, M. 2013a, *MNRAS*, 434, 633
- . 2013b, *MNRAS*, 428, L11
- Matthews, B., Kennedy, G., Sibthorpe, B., et al. 2014a, *ApJ*, 780, 97
- Matthews, B. C., Krivov, A. V., Wyatt, M. C., Bryden, G., & Eiroa, C. 2014b, *ArXiv e-prints*, arXiv:1401.0743
- McDonald, I., Zijlstra, A. A., & Boyer, M. L. 2012, *MNRAS*, 427, 343
- Meeus, G., Montesinos, B., Mendigutía, I., et al. 2012, *A&A*, 544, A78
- Min, M., Dullemond, C. P., Kama, M., & Dominik, C. 2011, *Icarus*, 212, 416
- Moór, A., Ábrahám, P., Derekas, A., et al. 2006, *ApJ*, 644, 525
- Moór, A., Apai, D., Pascucci, I., et al. 2009, *ApJL*, 700, L25
- Moór, A., Pascucci, I., Kóspál, Á., et al. 2011, *ApJS*, 193, 4
- Moór, A., Henning, T., Juhász, A., et al. 2015a, *ApJ*, 814, 42
- Moór, A., Kóspál, Á., Ábrahám, P., et al. 2015b, *MNRAS*, 447, 577
- Morales, F. Y., Bryden, G., Werner, M. W., & Stapelfeldt, K. R. 2013, *ApJ*, 776, 111
- Morales, F. Y., Rieke, G. H., Werner, M. W., et al. 2011, *ApJL*, 730, L29
- Muzerolle, J., Luhman, K. L., Briceño, C., Hartmann, L., & Calvet, N. 2005, *ApJ*, 625, 906
- Natta, A., Testi, L., & Randich, S. 2006, *A&A*, 452, 245
- Nesvorný, D., Jenniskens, P., Levison, H. F., et al. 2010, *ApJ*, 713, 816
- Nilsson, R., Liseau, R., Brandeker, A., et al. 2009, *A&A*, 508, 1057
- . 2010, *A&A*, 518, A40
- Olofsson, J., Samland, M., Avenhaus, H., et al. 2016, *A&A*, 591, A108
- Panić, O., Holland, W. S., Wyatt, M. C., et al. 2013, *MNRAS*, 435, 1037
- Pascual, N., Montesinos, B., Meeus, G., et al. 2016, *A&A*, 586, A6
- Pawellek, N., Krivov, A. V., Marshall, J. P., et al. 2014, *ApJ*, 792, 65
- Pecaut, M. J., & Mamajek, E. E. 2013, *ApJS*, 208, 9
- Petit, J.-M., Morbidelli, A., & Chambers, J. 2001, *Icarus*, 153, 338
- Ricarte, A., Moldvai, N., Hughes, A. M., et al. 2013, *ApJ*, 774, 80
- Ricci, L., Carpenter, J. M., Fu, B., et al. 2015a, *ApJ*, 798, 124
- Ricci, L., Maddison, S. T., Wilner, D., et al. 2015b, *ApJ*, 813, 138
- Rickman, H., Gabryszewski, R., Wajer, P., et al. 2017, *A&A*, 598, A110
- Rieke, G. H., Gáspár, A., & Ballering, N. P. 2016, *ApJ*, 816, 50
- Rieke, G. H., Young, E. T., Engelbracht, C. W., et al. 2004, *ApJS*, 154, 25
- Rieke, G. H., Su, K. Y. L., Stansberry, J. A., et al. 2005, *ApJ*, 620, 1010
- Riviere-Marichalar, P., Barrado, D., Montesinos, B., et al. 2014, *A&A*, 565, A68
- Roccatagliata, V., Henning, T., Wolf, S., et al. 2009, *A&A*, 497, 409
- Schneider, G., Silverstone, M. D., Hines, D. C., et al. 2006, *ApJ*, 650, 414
- Schneider, G., Grady, C. A., Hines, D. C., et al. 2014, *AJ*, 148, 59
- Schütz, O., Meeus, G., & Sterzik, M. F. 2005, *A&A*, 431, 175
- Sierchio, J. M., Rieke, G. H., Su, K. Y. L., & Gáspár, A. 2014, *ApJ*, 785, 33
- Stapelfeldt, K. R., Holmes, E. K., Chen, C., et al. 2004, *ApJS*, 154, 458
- Steele, A., Hughes, A. M., Carpenter, J., et al. 2016, *ApJ*, 816, 27
- Stevenson, D. J., & Lunine, J. I. 1988, *Icarus*, 75, 146
- Su, K. Y. L., & Rieke, G. H. 2014, in *IAU Symposium*, Vol. 299, IAU Symposium, ed. M. Booth, B. C. Matthews, & J. R. Graham, 318–321
- Su, K. Y. L., Rieke, G. H., Defrère, D., et al. 2016, *ApJ*, 818, 45
- Su, K. Y. L., Rieke, G. H., Stapelfeldt, K. R., et al. 2008, *ApJL*, 679, L125
- Su, K. Y. L., Rieke, G. H., Misselt, K. A., et al. 2005, *ApJ*, 628, 487
- Su, K. Y. L., Rieke, G. H., Stansberry, J. A., et al. 2006, *ApJ*, 653, 675
- Su, K. Y. L., Rieke, G. H., Stapelfeldt, K. R., et al. 2009, *ApJ*, 705, 314

- Su, K. Y. L., Rieke, G. H., Malhotra, R., et al. 2013, *ApJ*, 763, 118
- Tanner, A., Beichman, C., Bryden, G., Lisse, C., & Lawler, S. 2009, *ApJ*, 704, 109
- Thureau, N. D., Greaves, J. S., Matthews, B. C., et al. 2014, *MNRAS*, 445, 2558
- van Lieshout, R., Dominik, C., Kama, M., & Min, M. 2014, *A&A*, 571, A51
- Vican, L., Schneider, A., Bryden, G., et al. 2016, *ApJ*, 833, 263
- Williams, J. P., & Andrews, S. M. 2006, *ApJ*, 653, 1480
- Williams, J. P., Najita, J., Liu, M. C., et al. 2004, *ApJ*, 604, 414
- Wolf, S., & Voshchinnikov, N. V. 2004, *Computer Physics Communications*, 162, 113
- Wyatt, M. C. 2005, *A&A*, 433, 1007
- . 2008, *ARA&A*, 46, 339
- Wyatt, M. C., Smith, R., Greaves, J. S., et al. 2007, *ApJ*, 658, 569

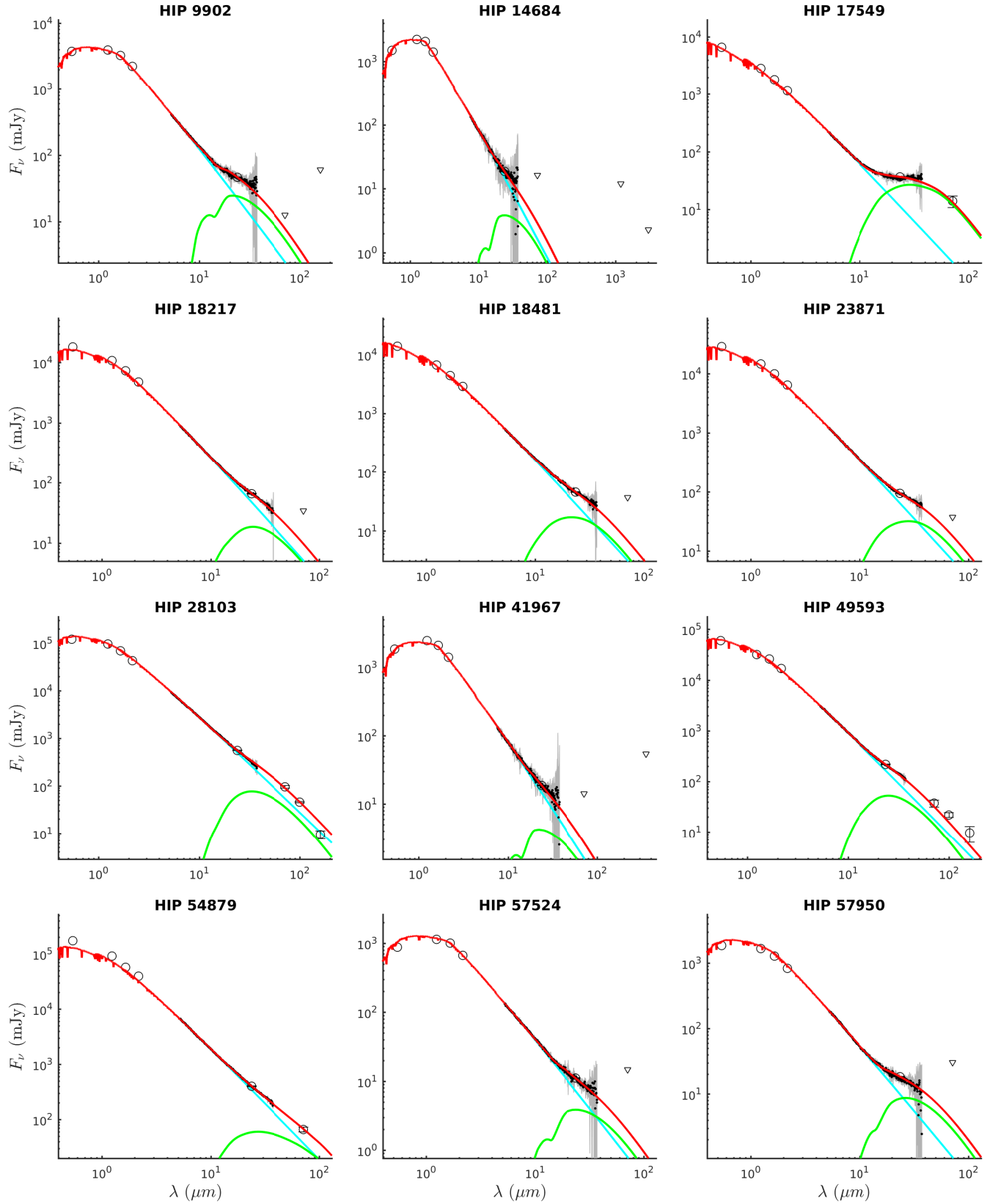


Figure 7. Best fits to the 29 single-component systems. Small black points are the IRS data (with gray error bars), large black circles are photometry data, and the black triangles are photometric upper limits. The stellar photosphere is cyan, the warm dust belt model is green, and the total model is red.

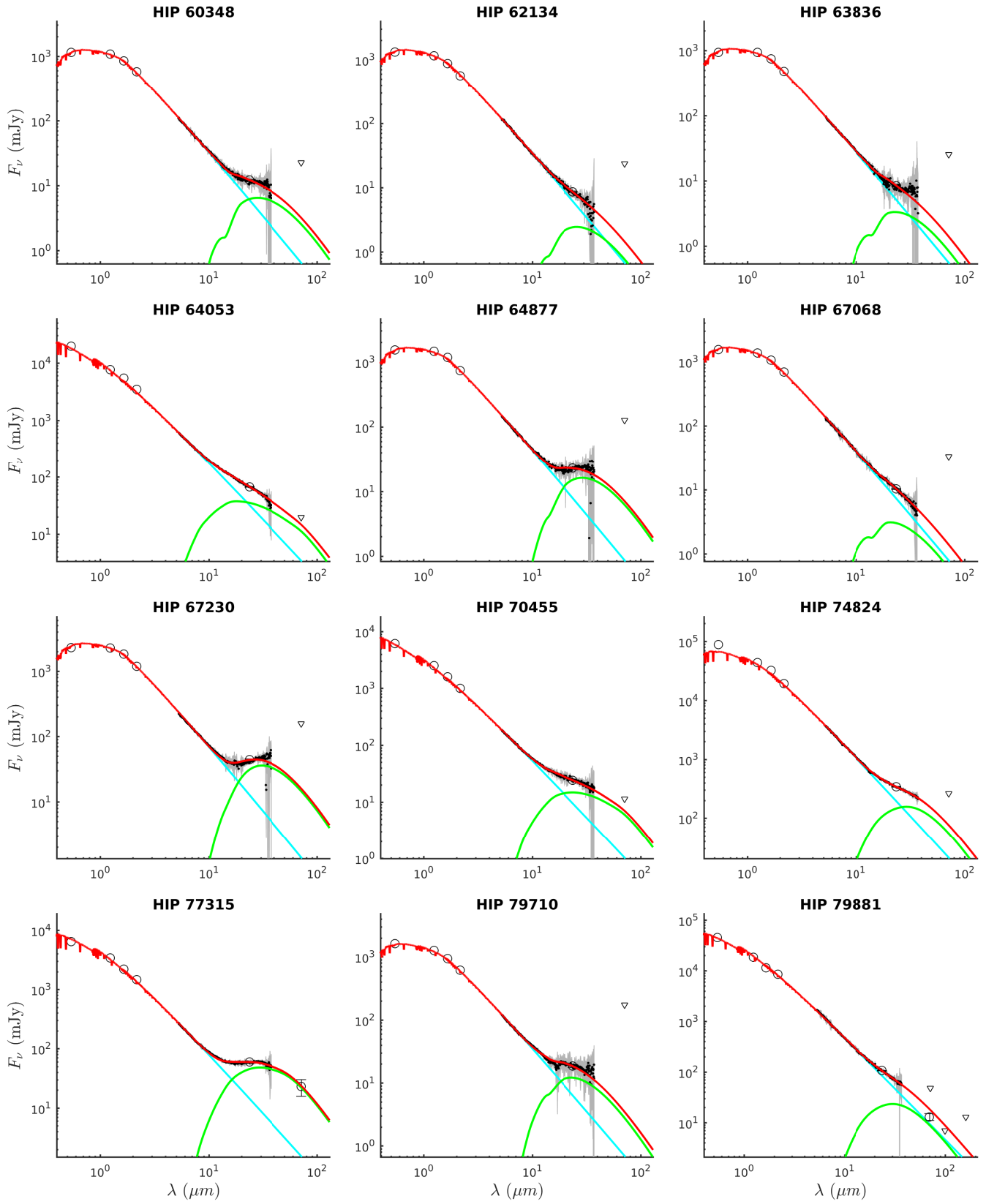


Figure 7. (continued).

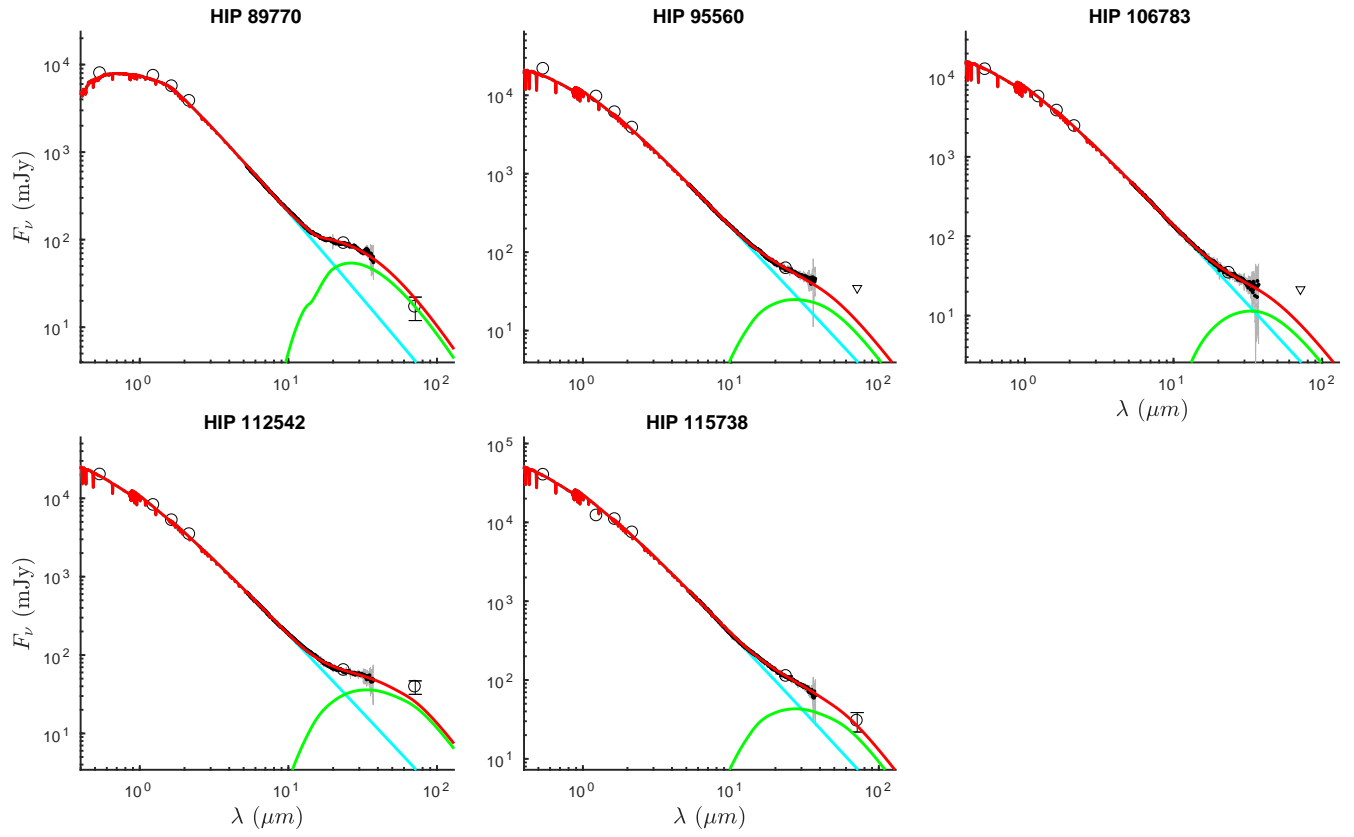


Figure 7. (continued).

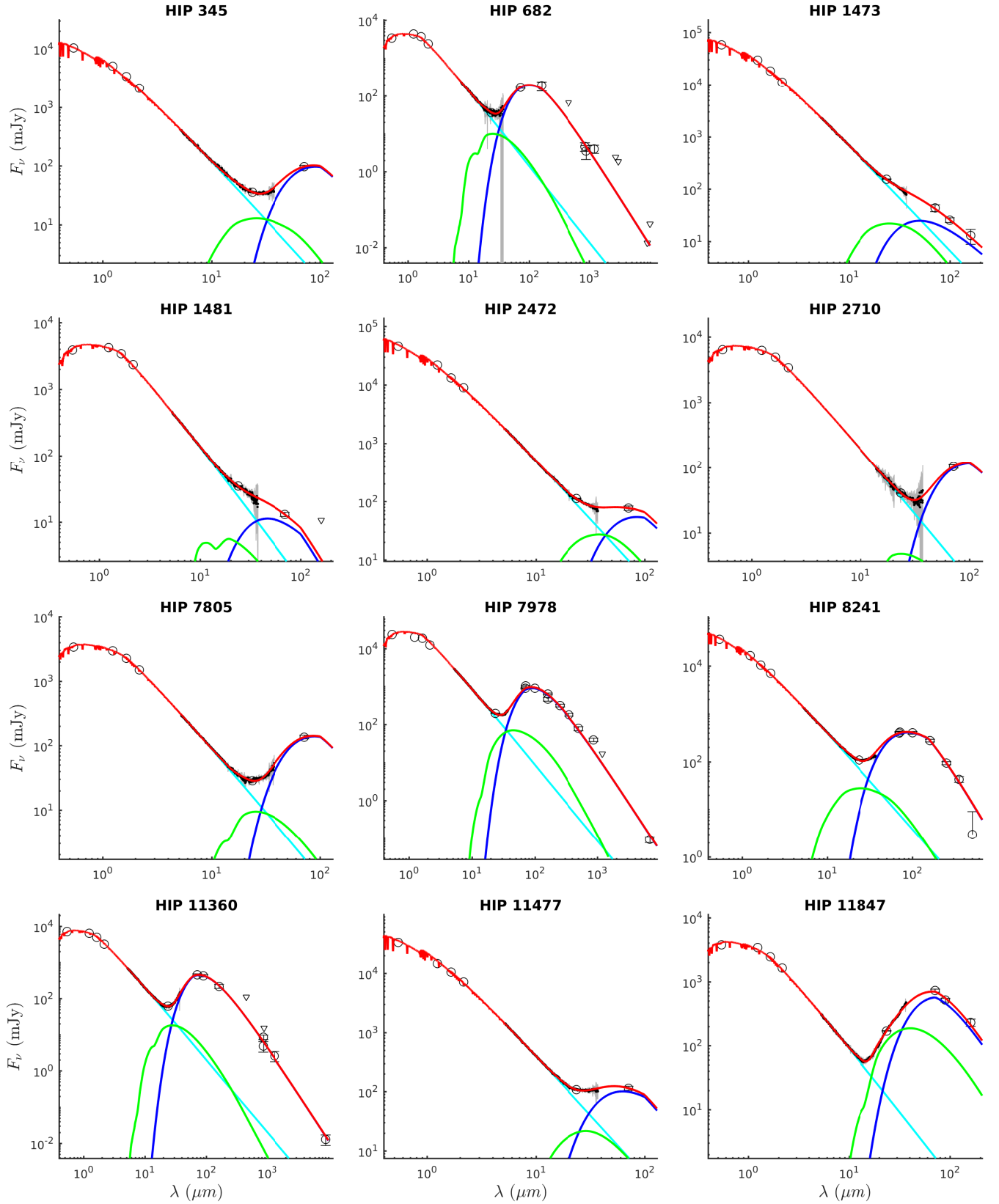


Figure 8. Best fits to the 54 two-component systems. Small black points are the IRS data (with gray error bars), large black circles are photometry data, and the black triangles are photometric upper limits. The stellar photosphere is cyan, the warm dust belt model is green, the cold component is blue, and the total model is red.

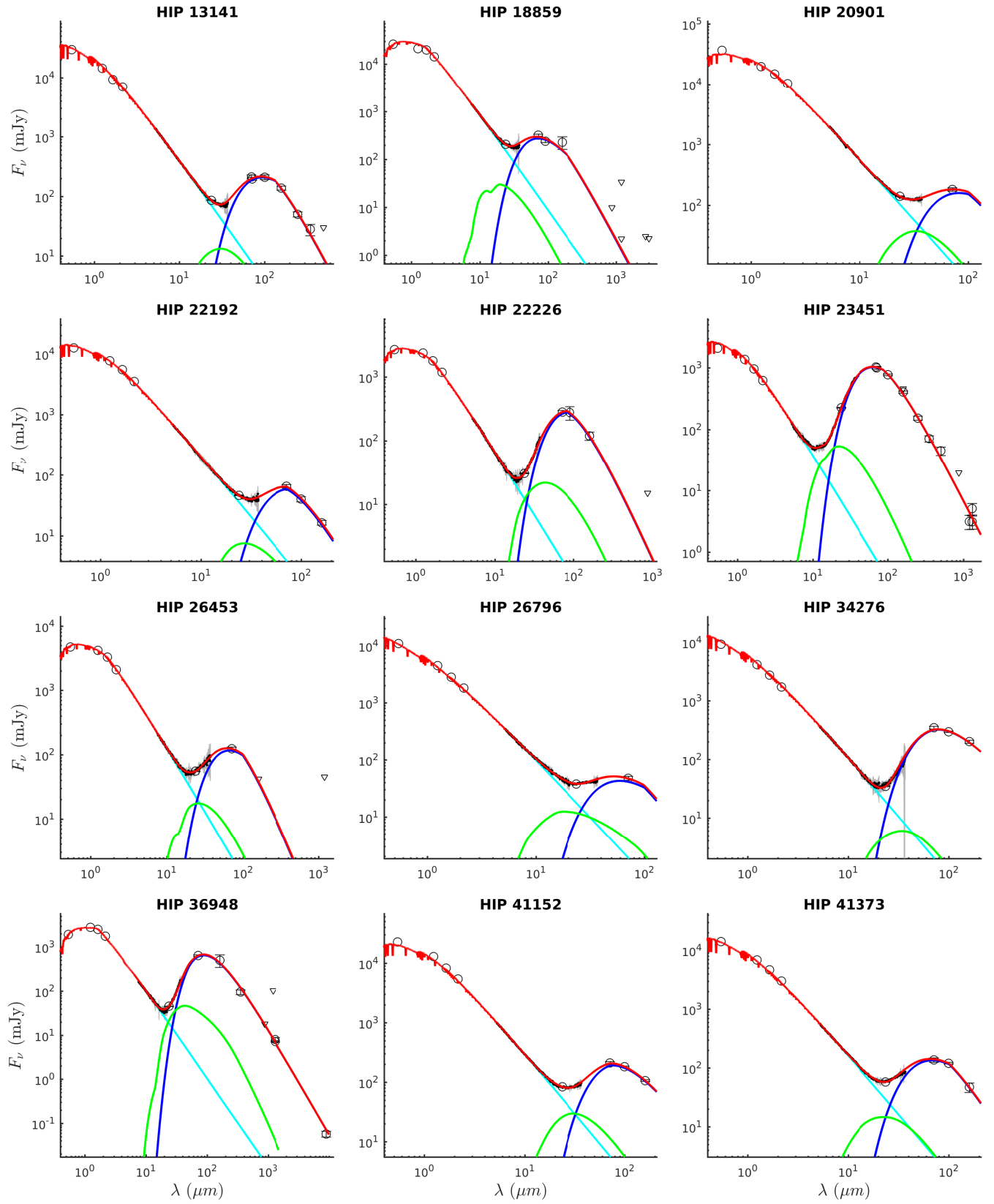


Figure 8. (continued).

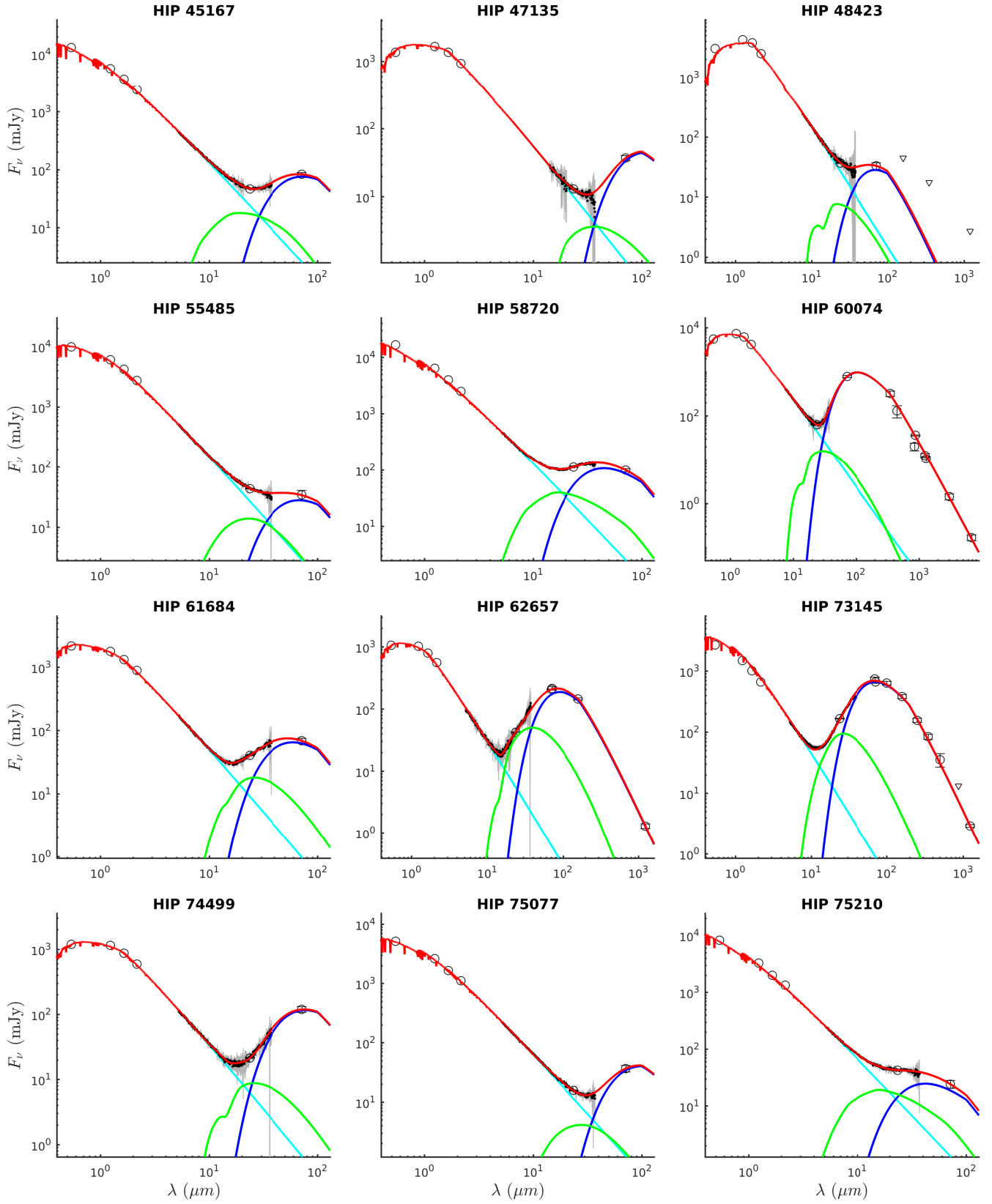


Figure 8. (continued).

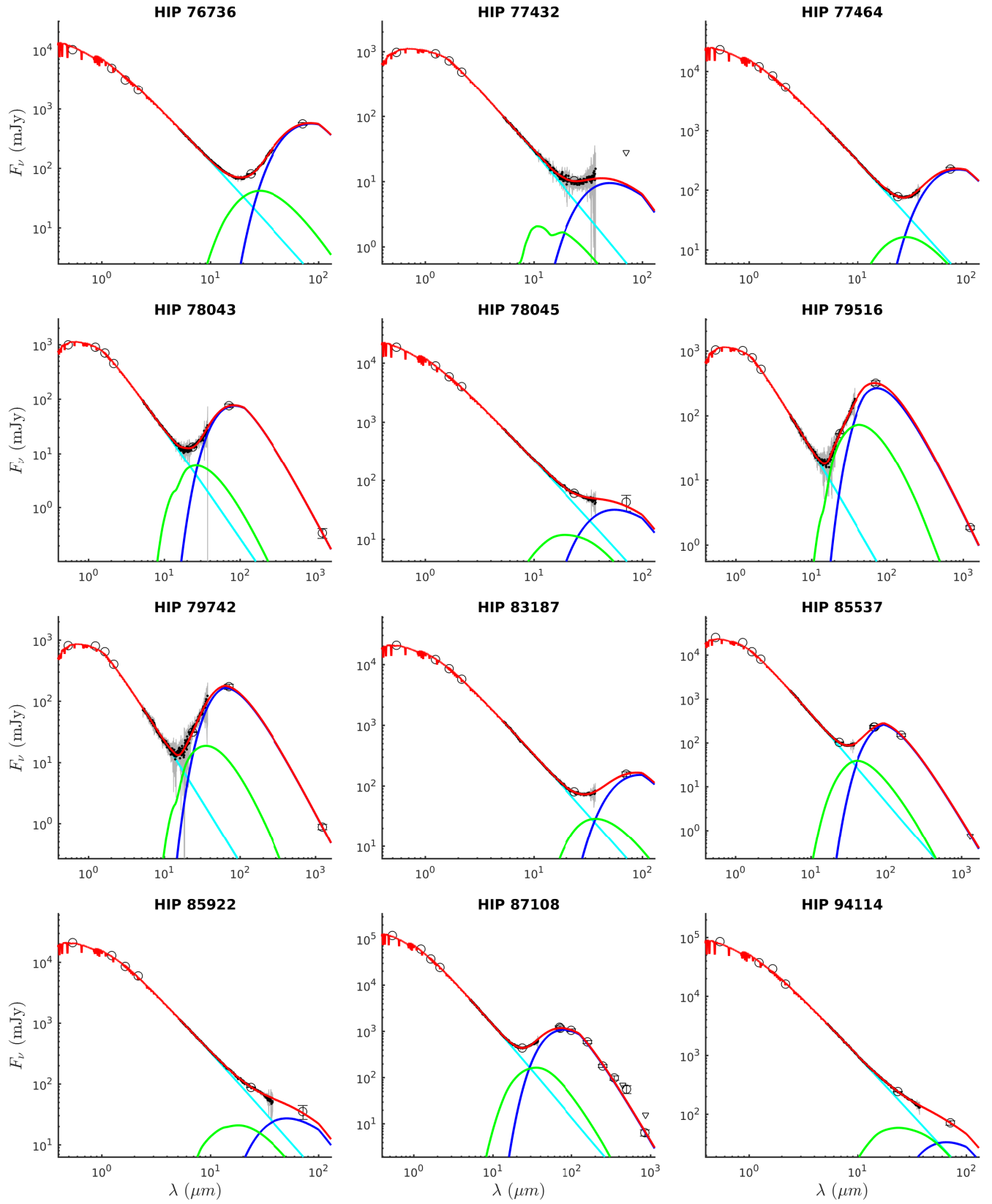


Figure 8. (continued).

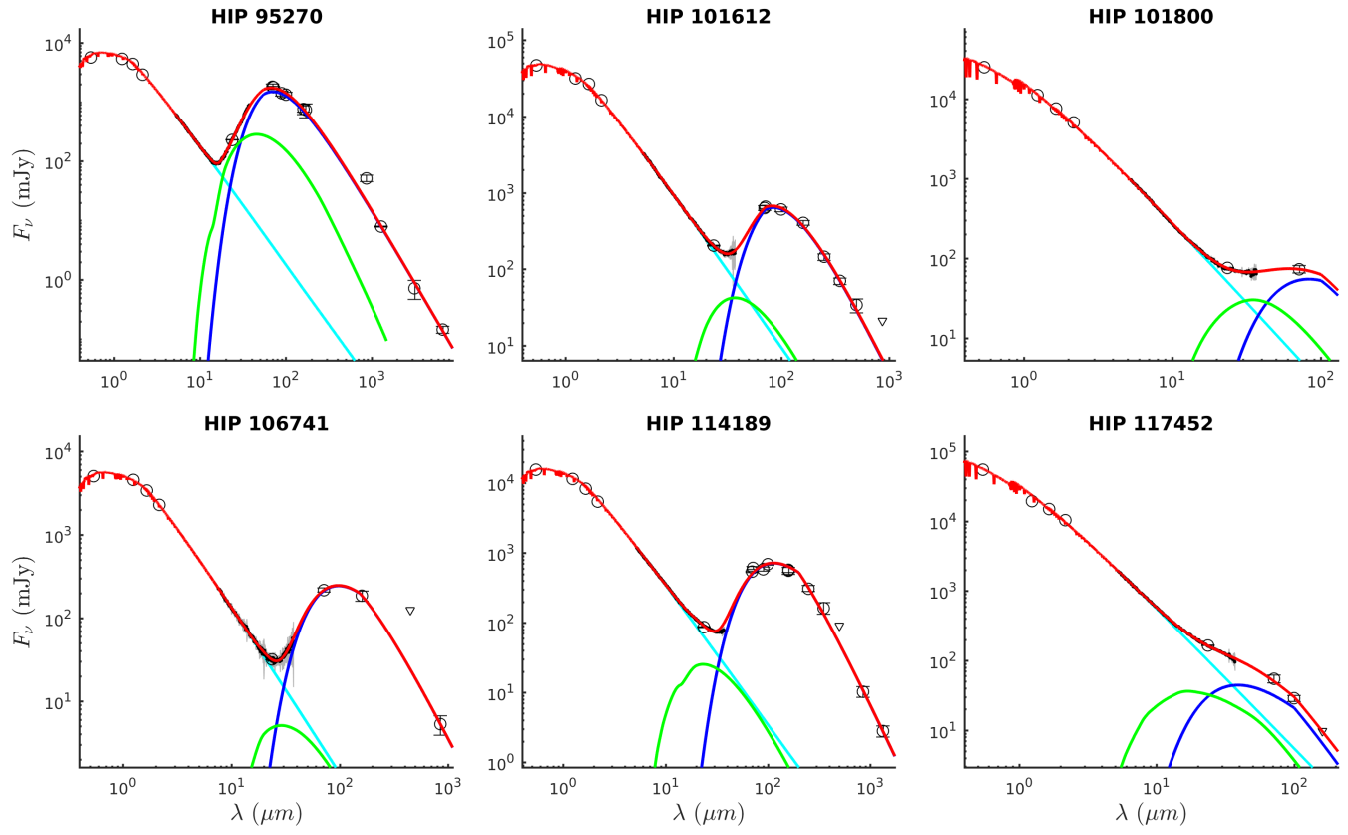


Figure 8. (continued).

Table 1. Target Properties

HIP Identifier	Spectral Type	V (mag)	J (mag)	H (mag)	K (mag)	T_* (K)	L_* (L_\odot)	M_* (M_\odot)	a_{BOS} (μm)	d (pc)	IRS AOR	x_{LL1}	x_{SL1}	x_{SL2}
Single-component Systems														
HIP 9902	F8V	7.5	6.53	6.3	6.2	6294	1.62	1.12	1	44.17	13621504	1.00	1.07	1.05
HIP 14684	G0V	8.49	7.16	6.79	6.7	5528	0.52	0.88	0.5	37.41	5340672	1.00	1.05	...
HIP 17549	A0	6.88	6.88	6.93	6.92	9820	34.15	2.26	7.5	140.84	14148096	0.94	1.19	1.08
HIP 18217	A5m	5.79	5.45	5.41	5.37	7667	9.73	1.69	3.1	50.51	14160640	1.00	1.02	1.02
HIP 18481	A2Vn	6.08	5.97	5.97	5.92	8801	15.12	1.88	4.2	70.22	14139648	0.99	1.00	0.99
HIP 23871	A5V	5.28	5.11	5.08	5.05	8308	20.32	2.01	5.2	58.11	14139904	1.00	1.10	1.06
HIP 28103 ^a	F2V	3.72	3.06	2.98	2.99	7207	7.88	1.60	2.7	14.88	15998720	1.00	1.04	1.04
HIP 41967	G5V	8.26	7.05	6.77	6.7	5875	0.89	0.99	0.7	45.07	6596864	0.94	1.00	...
HIP 49593	A7V	4.49	4.27	4.05	4	8000	9.98	1.70	3.2	28.24	14141184	1.00	1.06	1.00
HIP 54879	A2V	3.32	3.12	3.19	3.08	8080	92.43	2.92	15.5	50.61	16177152	1.00	1.00	1.00
HIP 57524	G4Vp	9.07	7.89	7.57	7.51	5887	1.75	1.14	1	91.66	21799936	1.00	1.06	1.04
HIP 57950	F2IV/V	8.25	7.47	7.31	7.28	6730	3.89	1.37	1.7	98.14	21800448	0.95	1.12	1.10
HIP 60348	F5V	8.78	7.95	7.76	7.67	6515	2.15	1.19	1.2	93.72	21801728	0.97	1.12	1.11
HIP 62134	F2V	8.63	7.88	7.73	7.71	6658	3.79	1.36	1.7	115.61	21802240	1.00	1.12	1.11
HIP 63836	F7	9	8.09	7.89	7.87	6501	2.41	1.23	1.3	107.41	21803008	1.00	1.13	1.11
HIP 64053	B8V	5.7	5.82	5.75	5.73	9800	51.38	2.52	10.1	100.1	22803712	1.00	1.03	1.02
HIP 64877	F5V	8.47	7.62	7.41	7.41	6448	5.21	1.47	2.1	125	22806784	1.00	1.07	1.07
HIP 67068	F3V	8.46	7.69	7.52	7.47	6787	2.82	1.27	1.4	91.58	26361856	1.00	0.99	0.96
HIP 67230	F5V	8.03	7.14	6.93	6.89	6476	8.73	1.65	2.9	131.75	22802688	1.00	1.08	1.08
HIP 70455	B8V	6.96	7.03	7.07	7.08	10460	48.73	2.49	9.7	165.02	14148608	1.00	1.02	1.00
HIP 74824	A3Va	4.07	3.93	3.81	3.88	7694	17.73	1.95	4.8	30.55	14141952	1.00	1.00	1.00
HIP 77315	A0V	6.92	6.69	6.72	6.67	8880	34.38	2.27	7.6	147.28	22804992	1.00	1.05	1.05
HIP 79710	F0V	8.4	7.77	7.65	7.61	7000	5.45	1.48	2.1	127.39	26314752	1.00	0.98	0.98
HIP 79881	A0V	4.79	4.86	4.94	4.74	9210	17.93	1.95	4.7	41.29	21809408	1.00	1.09	1.15
HIP 89770	F5	6.68	5.85	5.7	5.62	6599	4.87	1.44	2	53.22	15016960	1.00	1.00	0.99
HIP 95560	A0V	5.59	5.58	5.63	5.61	8673	25.02	2.11	6.1	72.89	14143488	0.98	1.04	1.04
HIP 106783	A2V	6.18	6.13	6.13	6.11	9158	22.37	2.05	5.6	87.64	21812992	0.99	1.10	1.11
HIP 112542	B9V	5.68	5.75	5.79	5.73	10016	50.69	2.51	10	97.37	14144000	1.00	1.05	1.05
HIP 115738 ^a	A0p...	4.93	5.32	4.98	4.9	9836	37.72	2.34	8.1	47.06	14144256	0.99	1.11	1.05
Two-component Systems														
HIP 345	A0V	6.39	6.28	6.25	6.26	8936	37.34	2.31	8.1	124.84	12720128	1.00	1.01	1.01
HIP 682	G2V	7.59	6.42	6.15	6.12	5962	1.23	1.05	0.8	39.08	5268736	1.00	1.07	...
HIP 1473	A2V	4.52	4.34	4.42	4.46	9005	22.94	2.06	5.7	41.32	14160384	1.00	1.03	1.03
HIP 1481	F9V	7.46	6.46	6.25	6.15	6273	1.50	1.10	0.9	41.55	21788160	0.97	1.07	1.06
HIP 2472 ^a	A0V	4.77	4.67	4.77	4.7	9459	29.59	2.22	6.7	52.97	21788672	1.00	1.09	1.11
HIP 2710	F2	6.91	6.04	5.85	5.75	6400	2.28	1.21	1.2	40.92	25673472	1.02
HIP 7805	F2IV/V	7.61	6.84	6.69	6.63	6796	3.27	1.32	1.5	67.25	21789952	1.00	1.13	1.11
HIP 7978	F9V	5.52	4.79	4.4	4.34	6000	1.58	1.11	1	17.43	16029952	0.99	1.05	1.06
HIP 8241	A1V	5.04	4.99	5.03	4.96	9478	32.98	2.25	7.4	62.03	14139392	1.00	1.06	1.04
HIP 11360	F2	6.8	6.03	5.86	5.82	6500	3.18	1.31	1.5	45.23	10885632	1.00	1.18	1.08
HIP 11477	A2V	5.13	5.12	5.03	4.94	8900	16.00	1.90	4.4	46.6	21790976	1.00	1.11	1.13
HIP 11847	F2V	7.49	6.7	6.61	6.55	6922	3.38	1.33	1.5	63.49	10886144	0.99	1.07	1.08
HIP 13141 ^a	A2V	5.26	5.14	5.16	4.97	8390	17.48	1.95	4.7	50.45	21791744	1.00	1.11	1.11

Table 1 continued

Table 1 (*continued*)

HIP Identifier	Spectral Type	V (mag)	J (mag)	H (mag)	K (mag)	T_* (K)	L_* (L_\odot)	M_* (M_\odot)	a_{BOS} (μm)	d (pc)	IRS AOR	x_{LL1}	x_{SL1}	x_{SL2}
HIP 18859 ^a	F5V	5.38	4.71	4.34	4.18	6315	2.59	1.24	1.3	18.83	5308416	1.00	1.01	...
HIP 20901	A7V	5.01	4.79	4.66	4.53	7592	17.44	1.94	4.7	48.85	14146816	1.00	1.03	1.03
HIP 22192	A3IV	6.18	5.8	5.73	5.71	7901	8.41	1.64	2.8	56.18	14147584	0.99	1.12	1.06
HIP 22226	F3V	7.86	7.1	6.95	6.89	6828	3.75	1.36	1.7	80.26	10887424	1.02	1.16	1.12
HIP 23451	A0	8.14	7.69	7.62	7.59	7957	6.19	1.53	2.3	112.36	15903744	1.00	1.05	1.12
HIP 26453	F3V	7.25	6.47	6.29	6.28	6758	3.28	1.32	1.5	56.79	5306880	1.00	1.08	...
HIP 26796	A0V	6.34	6.41	6.45	6.43	10130	69.94	2.72	12.6	153.61	12713728	0.99	1.10	1.07
HIP 34276	A0V	6.52	6.49	6.48	6.48	9400	23.76	2.08	5.8	102.35	21795584	1.00	1.07	1.07
HIP 36948	G8Vk+?	8.22	6.91	6.58	6.46	5598	0.61	0.91	0.5	35.35	5267200	1.00	1.02	...
HIP 41152	A3V	5.54	5.25	5.29	5.25	8077	12.05	1.78	3.6	50.43	14140416	1.00	1.10	1.06
HIP 41373	A0V	6.05	5.94	5.91	5.89	8839	15.39	1.88	4.3	69.44	14140672	1.00	1.12	1.08
HIP 45167	A0V	6.14	6.14	6.16	6.12	9152	29.56	2.19	6.8	99.3	12710400	1.00	1.04	1.03
HIP 47135	G2V	8.59	7.47	7.24	7.16	6050	1.46	1.09	0.9	67.98	25677056	1.00
HIP 48423	G5	7.73	6.47	6.14	6.09	5199	0.80	0.97	0.6	32.8	5399808	1.00	1.04	...
HIP 55485	A7Vn	6.44	6.08	6.02	5.99	8000	13.83	1.84	4	80.84	14141440	1.00	1.08	1.03
HIP 58720	B9V	5.88	6.01	6.08	6.08	10000	55.31	2.57	10.6	105.71	22799360	0.99	1.08	1.07
HIP 60074 ^a	G2V	7.07	5.87	5.61	5.54	5809	1.11	1.04	0.8	27.46	5312256	1.00	0.97	...
HIP 61684	A9V	8.09	7.41	7.27	7.2	7000	5.84	1.51	2.2	111.86	22801152	1.00	1.06	1.04
HIP 62657	F5/F6V	8.87	8	7.83	7.72	6417	2.65	1.25	1.3	108.58	13621248	1.01	1.06	1.05
HIP 73145	A2IV	7.86	7.6	7.56	7.52	8281	8.75	1.65	2.9	122.7	22803968	0.98	1.14	1.15
HIP 74499	F4V	8.74	7.88	7.73	7.65	6545	2.07	1.18	1.1	89.93	21806336	0.98	1.08	1.06
HIP 75077	A1V	7.16	6.98	7.04	6.96	8599	18.99	1.98	5	131.58	14151168	1.00	0.97	0.97
HIP 75210	B8/B9V	6.64	6.75	6.83	6.76	10642	45.95	2.45	9.3	136.24	14147840	1.00	1.05	1.04
HIP 76736	A1V	6.42	6.3	6.34	6.27	8769	13.56	1.83	3.9	78.49	14142208	1.00	1.10	1.12
HIP 77432	F5V	8.97	8.11	7.94	7.87	6594	1.98	1.17	1.1	96.34	21808128	1.00	1.12	1.10
HIP 77464	A5IV	5.53	5.33	5.27	5.26	8248	14.07	1.84	4	54.02	14142720	1.00	1.03	1.03
HIP 78043	F3V	8.95	8.15	7.97	7.94	6639	4.31	1.40	1.8	144.3	26313728	1.00	0.99	0.99
HIP 78045	A3V	5.75	5.65	5.66	5.57	8777	17.84	1.95	4.7	66.01	14142464	1.00	1.05	1.05
HIP 79516	F5V	8.9	8.02	7.85	7.79	6495	4.04	1.38	1.8	133.69	15554560	1.00	1.05	1.04
HIP 79742	F5	9.16	8.28	8.06	8.06	6516	3.80	1.36	1.7	146.2	15555328	1.00	1.00	0.98
HIP 83187	A5IV-V	5.65	5.32	5.26	5.19	7800	11.42	1.76	3.5	51.81	14160896	1.00	1.03	1.06
HIP 85537	A8V	5.42	4.81	4.88	4.8	7201	18.72	1.97	5	59.63	27224064	1.00	0.98	1.00
HIP 85922	A5V	5.62	5.25	5.25	5.14	7800	10.23	1.71	3.2	48.1	14142976	1.00	1.06	1.03
HIP 87108	A0V	3.75	3.59	3.66	3.62	8517	25.39	2.11	6.1	31.52	4931328	1.00	1.01	1.02
HIP 94114	A2Va	4.1	4.09	3.92	4.05	8400	26.47	2.13	6.3	38.43	14145536	1.00	1.05	1.01
HIP 95270	F5/F6V	7.04	6.2	5.98	5.91	6502	3.34	1.32	1.5	51.81	3564032	1.00	1.05	1.07
HIP 101612 ^a	F0V	4.76	4.28	4.02	4.04	7233	8.10	1.61	2.8	27.79	21812224	1.00	1.10	1.11
HIP 101800	A2V	5.43	5.41	5.37	5.3	9131	19.67	1.99	5.1	57.94	14161408	0.98	1.08	1.08
HIP 106741	F4IV	7.17	6.38	6.25	6.18	6786	2.92	1.28	1.4	51.81	15022592	1.00	1.10	...
HIP 114189	A5V	5.95	5.38	5.28	5.24	7033	4.82	1.44	2	39.4	28889856	1.00	1.00	1.00
HIP 117452 ^a	A0V	4.58	4.8	4.64	4.53	9673	33.98	2.29	7.4	42.14	14161664	1.00	1.02	1.02

^aThese targets not listed in McDonald et al. (2012); we inferred their stellar properties from their $V - K$ color.

Table 2. Target Photometry

HIP Identifier	λ (μm)	F_ν (mJy)	Instrument	References
Single-component Systems				
HIP 9902	24	46.67 ± 0.47	<i>Spitzer</i> /MIPS	Ballering et al. (2013)
HIP 9902	70	<12.56	<i>Spitzer</i> /MIPS	Ballering et al. (2013)
HIP 9902	160	<60.60	<i>Spitzer</i> /MIPS	Moór et al. (2009)
HIP 14684	24	18.68 ± 0.22	<i>Spitzer</i> /MIPS	Ballering et al. (2013)
HIP 14684	70	<16.38	<i>Spitzer</i> /MIPS	Ballering et al. (2013)
HIP 14684	1200	<12.00	SEST	Carpenter et al. (2005)
HIP 14684	3000	<2.30	OVRO	Carpenter et al. (2005)
HIP 17549	24	36.57 ± 0.40	<i>Spitzer</i> /MIPS	Ballering et al. (2013)
HIP 17549	70	13.95 ± 3.20	<i>Spitzer</i> /MIPS	Ballering et al. (2013)
HIP 18217	24	66.06 ± 0.68	<i>Spitzer</i> /MIPS	Ballering et al. (2013)
HIP 18217	70	<34.44	<i>Spitzer</i> /MIPS	Ballering et al. (2013)
HIP 18481	24	45.72 ± 0.49	<i>Spitzer</i> /MIPS	Ballering et al. (2013)
HIP 18481	70	<37.02	<i>Spitzer</i> /MIPS	Ballering et al. (2013)
HIP 23871	24	94.01 ± 0.98	<i>Spitzer</i> /MIPS	Ballering et al. (2013)
HIP 23871	70	<36.90	<i>Spitzer</i> /MIPS	Ballering et al. (2013)
HIP 28103	24	558.50 ± 5.67	<i>Spitzer</i> /MIPS	Ballering et al. (2013)
HIP 28103	70	95.96 ± 6.16	<i>Spitzer</i> /MIPS	Ballering et al. (2013)
HIP 28103	100	45.46 ± 1.42	<i>Herschel</i> /PACS	Eiroa et al. (2013)
HIP 28103	160	9.37 ± 1.84	<i>Herschel</i> /PACS	Eiroa et al. (2013)
HIP 41967	24	18.70 ± 0.22	<i>Spitzer</i> /MIPS	Ballering et al. (2013)
HIP 41967	70	<14.16	<i>Spitzer</i> /MIPS	Ballering et al. (2013)
HIP 41967	350	<54.00	CSO	Roccatagliata et al. (2009)
HIP 49593	24	218.20 ± 2.14	<i>Spitzer</i> /MIPS	Ballering et al. (2013)
HIP 49593	70	37.46 ± 5.99	<i>Spitzer</i> /MIPS	Ballering et al. (2013)
HIP 49593	100	22.07 ± 2.36	<i>Herschel</i> /PACS	Thureau et al. (2014)
HIP 49593	160	9.65 ± 3.40	<i>Herschel</i> /PACS	Thureau et al. (2014)
HIP 54879	24	401.10 ± 4.00	<i>Spitzer</i> /MIPS	Ballering et al. (2013)
HIP 54879	70	66.17 ± 6.28	<i>Spitzer</i> /MIPS	Ballering et al. (2013)
HIP 57524	24	11.11 ± 0.17	<i>Spitzer</i> /MIPS	Ballering et al. (2013)
HIP 57524	70	<14.80	<i>Spitzer</i> /MIPS	Ballering et al. (2013)
HIP 57950	24	18.41 ± 0.22	<i>Spitzer</i> /MIPS	Ballering et al. (2013)
HIP 57950	70	<30.51	<i>Spitzer</i> /MIPS	Ballering et al. (2013)
HIP 60348	24	12.18 ± 0.18	<i>Spitzer</i> /MIPS	Ballering et al. (2013)
HIP 60348	70	<22.70	<i>Spitzer</i> /MIPS	Ballering et al. (2013)
HIP 62134	24	8.59 ± 0.16	<i>Spitzer</i> /MIPS	Ballering et al. (2013)
HIP 62134	70	<23.62	<i>Spitzer</i> /MIPS	Ballering et al. (2013)
HIP 63836	24	8.40 ± 0.16	<i>Spitzer</i> /MIPS	Ballering et al. (2013)
HIP 63836	70	<25.19	<i>Spitzer</i> /MIPS	Ballering et al. (2013)
HIP 64053	24	67.32 ± 0.69	<i>Spitzer</i> /MIPS	Ballering et al. (2013)
HIP 64053	70	<19.81	<i>Spitzer</i> /MIPS	Ballering et al. (2013)
HIP 64877	24	22.88 ± 0.99	<i>Spitzer</i> /MIPS	Ballering et al. (2013)
HIP 64877	70	<126.60	<i>Spitzer</i> /MIPS	Ballering et al. (2013)
HIP 67068	24	10.25 ± 0.17	<i>Spitzer</i> /MIPS	Ballering et al. (2013)
HIP 67068	70	<33.48	<i>Spitzer</i> /MIPS	Ballering et al. (2013)
HIP 67230	24	44.09 ± 1.24	<i>Spitzer</i> /MIPS	Ballering et al. (2013)

Table 2 continued

Table 2 (*continued*)

HIP Identifier	λ (μm)	F_ν (mJy)	Instrument	References
HIP 67230	70	<157.98	<i>Spitzer</i> /MIPS	Ballering et al. (2013)
HIP 70455	24	24.25 \pm 0.33	<i>Spitzer</i> /MIPS	Ballering et al. (2013)
HIP 70455	70	<11.27	<i>Spitzer</i> /MIPS	Ballering et al. (2013)
HIP 74824	24	341.80 \pm 3.46	<i>Spitzer</i> /MIPS	Ballering et al. (2013)
HIP 74824	70	<263.58	<i>Spitzer</i> /MIPS	Ballering et al. (2013)
HIP 77315	24	59.61 \pm 0.60	<i>Spitzer</i> /MIPS	Ballering et al. (2013)
HIP 77315	70	22.92 \pm 7.22	<i>Spitzer</i> /MIPS	Ballering et al. (2013)
HIP 79710	24	18.61 \pm 1.07	<i>Spitzer</i> /MIPS	Ballering et al. (2013)
HIP 79710	70	<173.46	<i>Spitzer</i> /MIPS	Ballering et al. (2013)
HIP 79881	24	106.60 \pm 1.09	<i>Spitzer</i> /MIPS	Ballering et al. (2013)
HIP 79881	70	<47.88	<i>Spitzer</i> /MIPS	Ballering et al. (2013)
HIP 79881	70	13.00 \pm 2.00	<i>Herschel</i> /PACS	Riviere-Marichalar et al. (2014)
HIP 79881	100	<7.00	<i>Herschel</i> /PACS	Riviere-Marichalar et al. (2014)
HIP 79881	160	<13.00	<i>Herschel</i> /PACS	Riviere-Marichalar et al. (2014)
HIP 89770	24	90.66 \pm 0.90	<i>Spitzer</i> /MIPS	Ballering et al. (2013)
HIP 89770	70	16.99 \pm 5.08	<i>Spitzer</i> /MIPS	Ballering et al. (2013)
HIP 95560	24	61.84 \pm 0.65	<i>Spitzer</i> /MIPS	Ballering et al. (2013)
HIP 95560	70	<34.77	<i>Spitzer</i> /MIPS	Ballering et al. (2013)
HIP 106783	24	34.38 \pm 0.37	<i>Spitzer</i> /MIPS	Ballering et al. (2013)
HIP 106783	70	<21.42	<i>Spitzer</i> /MIPS	Ballering et al. (2013)
HIP 112542	24	63.92 \pm 0.66	<i>Spitzer</i> /MIPS	Ballering et al. (2013)
HIP 112542	70	39.17 \pm 7.65	<i>Spitzer</i> /MIPS	Ballering et al. (2013)
HIP 115738	24	111.70 \pm 1.12	<i>Spitzer</i> /MIPS	Ballering et al. (2013)
HIP 115738	70	30.27 \pm 8.38	<i>Spitzer</i> /MIPS	Ballering et al. (2013)
Two-component Systems				
HIP 345	24	35.70 \pm 0.38	<i>Spitzer</i> /MIPS	Ballering et al. (2013)
HIP 345	70	97.24 \pm 5.35	<i>Spitzer</i> /MIPS	Ballering et al. (2013)
HIP 682	24	36.49 \pm 0.39	<i>Spitzer</i> /MIPS	Ballering et al. (2013)
HIP 682	70	170.60 \pm 10.62	<i>Spitzer</i> /MIPS	Ballering et al. (2013)
HIP 682	160	187.50 \pm 50.40	<i>Spitzer</i> /MIPS	Hillenbrand et al. (2008)
HIP 682	450	<66.00	JCMT/SCUBA-2	Panić et al. (2013)
HIP 682	850	4.60 \pm 1.20	JCMT/SCUBA-2	Panić et al. (2013)
HIP 682	880	3.50 \pm 1.40	SMA	Steele et al. (2016)
HIP 682	1200	4.00 \pm 1.00	IRAM	Roccatagliata et al. (2009)
HIP 682	2700	<2.40	OVRO	Carpenter et al. (2005)
HIP 682	3000	<1.83	OVRO	Carpenter et al. (2005)
HIP 682	9000	<0.01	VLA	MacGregor et al. (2016)
HIP 682	10000	<0.04	GBT	Greaves et al. (2012)
HIP 1473	24	154.40 \pm 1.56	<i>Spitzer</i> /MIPS	Ballering et al. (2013)
HIP 1473	70	43.82 \pm 6.50	<i>Spitzer</i> /MIPS	Ballering et al. (2013)
HIP 1473	100	25.48 \pm 2.65	<i>Herschel</i> /PACS	Thureau et al. (2014)
HIP 1473	160	12.94 \pm 4.10	<i>Herschel</i> /PACS	Thureau et al. (2014)
HIP 1481	24	34.76 \pm 0.36	<i>Spitzer</i> /MIPS	Ballering et al. (2013)
HIP 1481	70	<	<i>Spitzer</i> /MIPS	Ballering et al. (2013)
HIP 1481	70	13.00 \pm 0.90	<i>Herschel</i> /PACS	Donaldson et al. (2012)
HIP 1481	160	<10.60	<i>Herschel</i> /PACS	Donaldson et al. (2012)
HIP 2472	24	112.50 \pm 1.12	<i>Spitzer</i> /MIPS	Ballering et al. (2013)
HIP 2472	70	76.98 \pm 6.54	<i>Spitzer</i> /MIPS	Ballering et al. (2013)

Table 2 *continued*

Table 2 (*continued*)

HIP Identifier	λ (μm)	F_ν (mJy)	Instrument	References
HIP 2710	24	40.62 ± 0.44	<i>Spitzer</i> /MIPS	Ballering et al. (2013)
HIP 2710	70	104.70 ± 6.50	<i>Spitzer</i> /MIPS	Ballering et al. (2013)
HIP 7805	24	28.74 ± 0.31	<i>Spitzer</i> /MIPS	Ballering et al. (2013)
HIP 7805	70	136.10 ± 9.30	<i>Spitzer</i> /MIPS	Ballering et al. (2013)
HIP 7978	24	196.20 ± 1.96	<i>Spitzer</i> /MIPS	Ballering et al. (2013)
HIP 7978	70	1035.00 ± 52.07	<i>Spitzer</i> /MIPS	Ballering et al. (2013)
HIP 7978	70	896.20 ± 26.90	<i>Herschel</i> /PACS	Eiroa et al. (2013)
HIP 7978	100	897.10 ± 26.90	<i>Herschel</i> /PACS	Eiroa et al. (2013)
HIP 7978	160	635.90 ± 31.80	<i>Herschel</i> /PACS	Eiroa et al. (2013)
HIP 7978	160	462.00 ± 50.00	<i>Spitzer</i> /MIPS	Tanner et al. (2009)
HIP 7978	250	312.30 ± 25.60	<i>Herschel</i> /SPIRE	Eiroa et al. (2013)
HIP 7978	350	179.90 ± 14.60	<i>Herschel</i> /SPIRE	Eiroa et al. (2013)
HIP 7978	500	78.40 ± 9.80	<i>Herschel</i> /SPIRE	Eiroa et al. (2013)
HIP 7978	870	39.40 ± 4.10	APEX/LABOCA	Liseau et al. (2008)
HIP 7978	1200	<17.00	SEST/SIMBA	Schütz et al. (2005)
HIP 7978	6800	0.09 ± 0.02	ATCA	Ricci et al. (2015b)
HIP 8241	24	108.30 ± 1.09	<i>Spitzer</i> /MIPS	Ballering et al. (2013)
HIP 8241	70	413.80 ± 21.54	<i>Spitzer</i> /MIPS	Ballering et al. (2013)
HIP 8241	70	396.00 ± 28.00	<i>Herschel</i> /PACS	Moór et al. (2015b)
HIP 8241	100	403.00 ± 28.00	<i>Herschel</i> /PACS	Moór et al. (2015b)
HIP 8241	160	277.00 ± 20.00	<i>Herschel</i> /PACS	Moór et al. (2015b)
HIP 8241	250	94.00 ± 7.00	<i>Herschel</i> /SPIRE	Moór et al. (2015b)
HIP 8241	350	43.00 ± 6.00	<i>Herschel</i> /SPIRE	Moór et al. (2015b)
HIP 8241	500	3.00 ± 6.00	<i>Herschel</i> /SPIRE	Moór et al. (2015b)
HIP 11360	24	60.87 ± 0.64	<i>Spitzer</i> /MIPS	Ballering et al. (2013)
HIP 11360	70	454.30 ± 24.37	<i>Spitzer</i> /MIPS	Ballering et al. (2013)
HIP 11360	90	427.00 ± 30.00	<i>ISO</i>	Moór et al. (2006)
HIP 11360	160	217.30 ± 27.80	<i>Spitzer</i> /MIPS	Moór et al. (2011)
HIP 11360	450	<111.00	JCMT/SCUBA-2	Panić et al. (2013)
HIP 11360	850	8.50 ± 1.20	JCMT/SCUBA-2	Panić et al. (2013)
HIP 11360	850	4.90 ± 1.60	JCMT/SCUBA	Williams & Andrews (2006)
HIP 11360	870	<15.30	APEX/LABOCA	Nilsson et al. (2009)
HIP 11360	1300	2.60 ± 0.80	SMA	MacGregor et al. (2015)
HIP 11360	9000	0.01 ± 0.00	VLA	MacGregor et al. (2016)
HIP 11477	24	108.60 ± 1.06	<i>Spitzer</i> /MIPS	Ballering et al. (2013)
HIP 11477	70	114.70 ± 8.81	<i>Spitzer</i> /MIPS	Ballering et al. (2013)
HIP 11847	24	170.10 ± 1.71	<i>Spitzer</i> /MIPS	Ballering et al. (2013)
HIP 11847	70	722.90 ± 36.80	<i>Spitzer</i> /MIPS	Ballering et al. (2013)
HIP 11847	90	515.00 ± 36.00	<i>ISO</i>	Moór et al. (2006)
HIP 11847	160	230.80 ± 29.90	<i>Spitzer</i> /MIPS	Moór et al. (2011)
HIP 13141	24	86.22 ± 0.88	<i>Spitzer</i> /MIPS	Ballering et al. (2013)
HIP 13141	70	197.10 ± 11.61	<i>Spitzer</i> /MIPS	Ballering et al. (2013)
HIP 13141	70	213.00 ± 17.00	<i>Herschel</i> /PACS	Moór et al. (2015b)
HIP 13141	100	210.00 ± 18.00	<i>Herschel</i> /PACS	Moór et al. (2015b)
HIP 13141	160	138.00 ± 11.00	<i>Herschel</i> /PACS	Moór et al. (2015b)
HIP 13141	250	50.00 ± 5.00	<i>Herschel</i> /SPIRE	Moór et al. (2015b)
HIP 13141	350	28.00 ± 6.00	<i>Herschel</i> /SPIRE	Moór et al. (2015b)
HIP 13141	500	<30.00	<i>Herschel</i> /SPIRE	Moór et al. (2015b)
HIP 18859	24	207.90 ± 2.02	<i>Spitzer</i> /MIPS	Ballering et al. (2013)
HIP 18859	70	321.70 ± 16.92	<i>Spitzer</i> /MIPS	Ballering et al. (2013)

Table 2 continued

Table 2 (*continued*)

HIP Identifier	λ (μm)	F_ν (mJy)	Instrument	References
HIP 18859	90	242.00 \pm 18.00	<i>ISO</i>	Moór et al. (2006)
HIP 18859	160	229.40 \pm 67.50	<i>Spitzer</i> /MIPS	Hillenbrand et al. (2008)
HIP 18859	870	<9.90	APEX/LABOCA	Nilsson et al. (2010)
HIP 18859	1200	<34.00	SEST	Carpenter et al. (2005)
HIP 18859	1200	<2.20	IRAM	Roccatagliata et al. (2009)
HIP 18859	2700	<2.48	OVRO	Carpenter et al. (2005)
HIP 18859	3000	<2.23	OVRO	Carpenter et al. (2005)
HIP 20901	24	140.60 \pm 1.40	<i>Spitzer</i> /MIPS	Ballering et al. (2013)
HIP 20901	70	182.50 \pm 11.21	<i>Spitzer</i> /MIPS	Ballering et al. (2013)
HIP 22192	24	46.17 \pm 0.47	<i>Spitzer</i> /MIPS	Ballering et al. (2013)
HIP 22192	70	65.54 \pm 3.92	<i>Spitzer</i> /MIPS	Ballering et al. (2013)
HIP 22192	100	40.20 \pm 3.80	<i>Herschel</i> /PACS	Draper et al. (2016a)
HIP 22192	160	16.40 \pm 1.50	<i>Herschel</i> /PACS	Draper et al. (2016a)
HIP 22226	24	30.61 \pm 0.30	<i>Spitzer</i> /MIPS	Ballering et al. (2013)
HIP 22226	70	283.30 \pm 15.33	<i>Spitzer</i> /MIPS	Ballering et al. (2013)
HIP 22226	90	277.00 \pm 67.00	<i>ISO</i>	Moór et al. (2006)
HIP 22226	160	120.30 \pm 17.60	<i>Spitzer</i> /MIPS	Moór et al. (2011)
HIP 22226	870	<15.00	APEX/LABOCA	Nilsson et al. (2010)
HIP 23451	24	226.20 \pm 2.26	<i>Spitzer</i> /MIPS	Ballering et al. (2013)
HIP 23451	70	1003.00 \pm 50.55	<i>Spitzer</i> /MIPS	Ballering et al. (2013)
HIP 23451	70	1038.00 \pm 29.00	<i>Herschel</i> /PACS	Donaldson et al. (2013)
HIP 23451	100	770.00 \pm 22.00	<i>Herschel</i> /PACS	Donaldson et al. (2013)
HIP 23451	160	403.00 \pm 20.00	<i>Herschel</i> /PACS	Donaldson et al. (2013)
HIP 23451	160	<460.00	<i>Spitzer</i> /MIPS	Maness et al. (2008)
HIP 23451	250	153.00 \pm 12.00	<i>Herschel</i> /SPIRE	Donaldson et al. (2013)
HIP 23451	350	71.00 \pm 8.00	<i>Herschel</i> /SPIRE	Donaldson et al. (2013)
HIP 23451	500	45.00 \pm 7.00	<i>Herschel</i> /SPIRE	Donaldson et al. (2013)
HIP 23451	870	<19.50	APEX/LABOCA	Nilsson et al. (2010)
HIP 23451	1200	3.14 \pm 0.82	IRAM/MAMBO2	Meeus et al. (2012)
HIP 23451	1300	3.10 \pm 0.74	SMA	Meeus et al. (2012)
HIP 23451	1300	5.10 \pm 1.10	CARMA	Maness et al. (2008)
HIP 26453	24	55.16 \pm 0.54	<i>Spitzer</i> /MIPS	Ballering et al. (2013)
HIP 26453	70	123.30 \pm 7.80	<i>Spitzer</i> /MIPS	Ballering et al. (2013)
HIP 26453	160	<42.00	<i>Spitzer</i> /MIPS	Hillenbrand et al. (2008)
HIP 26453	1200	<45.00	SEST	Carpenter et al. (2005)
HIP 26796	24	37.66 \pm 0.39	<i>Spitzer</i> /MIPS	Ballering et al. (2013)
HIP 26796	70	47.92 \pm 4.19	<i>Spitzer</i> /MIPS	Ballering et al. (2013)
HIP 34276	24	34.76 \pm 0.37	<i>Spitzer</i> /MIPS	Ballering et al. (2013)
HIP 34276	70	348.70 \pm 18.23	<i>Spitzer</i> /MIPS	Ballering et al. (2013)
HIP 34276	100	297.00 \pm 8.90	<i>Herschel</i> /PACS	Vican et al. (2016)
HIP 34276	160	200.00 \pm 11.00	<i>Herschel</i> /PACS	Vican et al. (2016)
HIP 36948	24	45.24 \pm 0.47	<i>Spitzer</i> /MIPS	Ballering et al. (2013)
HIP 36948	70	636.20 \pm 32.40	<i>Spitzer</i> /MIPS	Ballering et al. (2013)
HIP 36948	160	502.60 \pm 160.10	<i>Spitzer</i> /MIPS	Hillenbrand et al. (2008)
HIP 36948	350	95.00 \pm 12.00	CSO	Roccatagliata et al. (2009)
HIP 36948	870	<18.00	APEX/LABOCA	Nilsson et al. (2010)
HIP 36948	1200	<102.00	SEST	Carpenter et al. (2005)
HIP 36948	1300	7.98 \pm 0.80	SMA	Steele et al. (2016)
HIP 36948	1300	7.20 \pm 0.30	SMA	Ricarte et al. (2013)
HIP 36948	9000	0.06 \pm 0.01	VLA	MacGregor et al. (2016)

Table 2 continued

Table 2 (*continued*)

HIP Identifier	λ (μm)	F_ν (mJy)	Instrument	References
HIP 41152	24	83.30 ± 0.82	<i>Spitzer</i> /MIPS	Ballering et al. (2013)
HIP 41152	70	209.70 ± 12.17	<i>Spitzer</i> /MIPS	Ballering et al. (2013)
HIP 41152	100	181.30 ± 4.80	<i>Herschel</i> /PACS	Morales et al. (2013)
HIP 41152	160	106.70 ± 3.90	<i>Herschel</i> /PACS	Morales et al. (2013)
HIP 41373	24	57.73 ± 0.59	<i>Spitzer</i> /MIPS	Ballering et al. (2013)
HIP 41373	70	136.70 ± 11.69	<i>Spitzer</i> /MIPS	Ballering et al. (2013)
HIP 41373	100	120.50 ± 4.10	<i>Herschel</i> /PACS	Morales et al. (2013)
HIP 41373	160	46.90 ± 8.70	<i>Herschel</i> /PACS	Morales et al. (2013)
HIP 45167	24	46.51 ± 0.49	<i>Spitzer</i> /MIPS	Ballering et al. (2013)
HIP 45167	70	82.85 ± 5.37	<i>Spitzer</i> /MIPS	Ballering et al. (2013)
HIP 47135	24	12.93 ± 0.13	<i>Spitzer</i> /MIPS	Ballering et al. (2013)
HIP 47135	70	36.90 ± 3.27	<i>Spitzer</i> /MIPS	Ballering et al. (2013)
HIP 48423	24	36.88 ± 0.38	<i>Spitzer</i> /MIPS	Ballering et al. (2013)
HIP 48423	70	33.09 ± 4.36	<i>Spitzer</i> /MIPS	Ballering et al. (2013)
HIP 48423	160	<44.80	<i>Spitzer</i> /MIPS	Hillenbrand et al. (2008)
HIP 48423	350	<17.40	CSO	Roccatagliata et al. (2009)
HIP 48423	1200	<2.70	IRAM	Roccatagliata et al. (2009)
HIP 55485	24	43.52 ± 0.45	<i>Spitzer</i> /MIPS	Ballering et al. (2013)
HIP 55485	70	34.45 ± 6.17	<i>Spitzer</i> /MIPS	Ballering et al. (2013)
HIP 58720	24	111.70 ± 1.10	<i>Spitzer</i> /MIPS	Ballering et al. (2013)
HIP 58720	70	98.53 ± 6.32	<i>Spitzer</i> /MIPS	Ballering et al. (2013)
HIP 60074	24	62.86 ± 0.64	<i>Spitzer</i> /MIPS	Ballering et al. (2013)
HIP 60074	70	782.20 ± 39.62	<i>Spitzer</i> /MIPS	Ballering et al. (2013)
HIP 60074	350	319.00 ± 45.00	CSO	Corder et al. (2009)
HIP 60074	450	130.00 ± 40.00	JCMT/SCUBA	Williams et al. (2004)
HIP 60074	850	20.00 ± 4.00	JCMT/SCUBA	Williams et al. (2004)
HIP 60074	880	36.00 ± 1.00	SMA	Hughes et al. (2011)
HIP 60074	1250	12.50 ± 1.30	ALMA	Ricci et al. (2015a)
HIP 60074	1300	10.40 ± 1.40	CARMA	Corder et al. (2009)
HIP 60074	3000	1.42 ± 0.23	OVRO	Carpenter et al. (2005)
HIP 60074	6800	0.17 ± 0.03	ATCA	Ricci et al. (2015b)
HIP 61684	24	40.59 ± 0.42	<i>Spitzer</i> /MIPS	Ballering et al. (2013)
HIP 61684	70	69.02 ± 6.09	<i>Spitzer</i> /MIPS	Ballering et al. (2013)
HIP 62657	24	42.34 ± 0.43	<i>Spitzer</i> /MIPS	Ballering et al. (2013)
HIP 62657	70	214.80 ± 13.39	<i>Spitzer</i> /MIPS	Ballering et al. (2013)
HIP 62657	70	205.00 ± 4.00	<i>Herschel</i> /PACS	Draper et al. (2016b)
HIP 62657	160	145.00 ± 6.00	<i>Herschel</i> /PACS	Draper et al. (2016b)
HIP 62657	1240	1.29 ± 0.11	ALMA	Liemman-Sifry et al. (2016)
HIP 73145	24	166.60 ± 1.67	<i>Spitzer</i> /MIPS	Ballering et al. (2013)
HIP 73145	70	659.20 ± 33.40	<i>Spitzer</i> /MIPS	Ballering et al. (2013)
HIP 73145	70	738.70 ± 52.50	<i>Herschel</i> /PACS	Moór et al. (2015a)
HIP 73145	100	637.00 ± 45.50	<i>Herschel</i> /PACS	Moór et al. (2015a)
HIP 73145	160	382.30 ± 27.90	<i>Herschel</i> /PACS	Moór et al. (2015a)
HIP 73145	250	156.40 ± 11.50	<i>Herschel</i> /SPIRE	Moór et al. (2015a)
HIP 73145	350	84.30 ± 8.30	<i>Herschel</i> /SPIRE	Moór et al. (2015a)
HIP 73145	500	35.40 ± 8.90	<i>Herschel</i> /SPIRE	Moór et al. (2015a)
HIP 73145	870	<13.20	APEX/LABOCA	Nilsson et al. (2010)
HIP 73145	1240	2.90 ± 0.15	ALMA	Liemman-Sifry et al. (2016)
HIP 74499	24	21.42 ± 0.27	<i>Spitzer</i> /MIPS	Ballering et al. (2013)
HIP 74499	70	118.80 ± 11.85	<i>Spitzer</i> /MIPS	Ballering et al. (2013)

Table 2 continued

Table 2 (*continued*)

HIP Identifier	λ (μm)	F_ν (mJy)	Instrument	References
HIP 75077	24	15.64 ± 0.24	<i>Spitzer</i> /MIPS	Ballering et al. (2013)
HIP 75077	70	36.80 ± 4.64	<i>Spitzer</i> /MIPS	Ballering et al. (2013)
HIP 75210	24	42.33 ± 0.46	<i>Spitzer</i> /MIPS	Ballering et al. (2013)
HIP 75210	70	24.20 ± 3.74	<i>Spitzer</i> /MIPS	Ballering et al. (2013)
HIP 76736	24	80.67 ± 0.82	<i>Spitzer</i> /MIPS	Ballering et al. (2013)
HIP 76736	70	560.60 ± 29.29	<i>Spitzer</i> /MIPS	Ballering et al. (2013)
HIP 77432	24	10.28 ± 0.19	<i>Spitzer</i> /MIPS	Ballering et al. (2013)
HIP 77432	70	<27.93	<i>Spitzer</i> /MIPS	Ballering et al. (2013)
HIP 77464	24	78.32 ± 0.81	<i>Spitzer</i> /MIPS	Ballering et al. (2013)
HIP 77464	70	224.90 ± 14.34	<i>Spitzer</i> /MIPS	Ballering et al. (2013)
HIP 78043	24	13.14 ± 0.16	<i>Spitzer</i> /MIPS	Ballering et al. (2013)
HIP 78043	70	75.36 ± 6.32	<i>Spitzer</i> /MIPS	Ballering et al. (2013)
HIP 78043	1240	0.34 ± 0.07	ALMA	Lieman-Sifry et al. (2016)
HIP 78045	24	60.25 ± 0.63	<i>Spitzer</i> /MIPS	Ballering et al. (2013)
HIP 78045	70	42.95 ± 13.02	<i>Spitzer</i> /MIPS	Ballering et al. (2013)
HIP 79516	24	52.88 ± 0.57	<i>Spitzer</i> /MIPS	Ballering et al. (2013)
HIP 79516	70	317.20 ± 25.71	<i>Spitzer</i> /MIPS	Ballering et al. (2013)
HIP 79516	1240	1.85 ± 0.12	ALMA	Lieman-Sifry et al. (2016)
HIP 79742	24	31.15 ± 0.34	<i>Spitzer</i> /MIPS	Ballering et al. (2013)
HIP 79742	70	173.00 ± 16.28	<i>Spitzer</i> /MIPS	Ballering et al. (2013)
HIP 79742	1240	0.88 ± 0.09	ALMA	Lieman-Sifry et al. (2016)
HIP 83187	24	80.34 ± 0.80	<i>Spitzer</i> /MIPS	Ballering et al. (2013)
HIP 83187	70	156.60 ± 13.89	<i>Spitzer</i> /MIPS	Ballering et al. (2013)
HIP 85537	24	103.10 ± 1.03	<i>Spitzer</i> /MIPS	Ballering et al. (2013)
HIP 85537	70	229.10 ± 11.90	<i>Spitzer</i> /MIPS	Ballering et al. (2013)
HIP 85537	70	230.00 ± 20.00	<i>Herschel</i> /PACS	Pascual et al. (2016)
HIP 85537	160	150.00 ± 10.00	<i>Herschel</i> /PACS	Pascual et al. (2016)
HIP 85537	1300	<0.75	SMA	Meeus et al. (2012)
HIP 85922	24	87.64 ± 0.88	<i>Spitzer</i> /MIPS	Ballering et al. (2013)
HIP 85922	70	35.21 ± 9.07	<i>Spitzer</i> /MIPS	Ballering et al. (2013)
HIP 87108	24	434.10 ± 4.34	<i>Spitzer</i> /MIPS	Ballering et al. (2013)
HIP 87108	70	1166.00 ± 58.37	<i>Spitzer</i> /MIPS	Ballering et al. (2013)
HIP 87108	70	1222.00 ± 85.00	<i>Herschel</i> /PACS	Moór et al. (2015b)
HIP 87108	100	1051.00 ± 73.00	<i>Herschel</i> /PACS	Moór et al. (2015b)
HIP 87108	160	587.00 ± 44.00	<i>Herschel</i> /PACS	Moór et al. (2015b)
HIP 87108	250	177.00 ± 12.00	<i>Herschel</i> /SPIRE	Moór et al. (2015b)
HIP 87108	350	98.00 ± 10.00	<i>Herschel</i> /SPIRE	Moór et al. (2015b)
HIP 87108	450	<69.00	JCMT/SCUBA-2	Panić et al. (2013)
HIP 87108	500	56.00 ± 11.00	<i>Herschel</i> /SPIRE	Moór et al. (2015b)
HIP 87108	850	6.40 ± 1.00	JCMT/SCUBA-2	Panić et al. (2013)
HIP 87108	870	<15.60	APEX/LABOCA	Nilsson et al. (2010)
HIP 94114	24	240.00 ± 2.40	<i>Spitzer</i> /MIPS	Ballering et al. (2013)
HIP 94114	70	70.92 ± 5.92	<i>Spitzer</i> /MIPS	Ballering et al. (2013)
HIP 95270	24	230.30 ± 2.31	<i>Spitzer</i> /MIPS	Ballering et al. (2013)
HIP 95270	70	1776.00 ± 89.31	<i>Spitzer</i> /MIPS	Ballering et al. (2013)
HIP 95270	70	1827.00 ± 183.00	<i>Herschel</i> /PACS	Lebreton et al. (2012)
HIP 95270	90	1410.00 ± 140.00	<i>ISO</i>	Moór et al. (2006)
HIP 95270	100	1337.00 ± 134.00	<i>Herschel</i> /PACS	Lebreton et al. (2012)
HIP 95270	160	767.00 ± 153.00	<i>Herschel</i> /PACS	Lebreton et al. (2012)
HIP 95270	160	770.00 ± 90.00	<i>Spitzer</i> /MIPS	Schneider et al. (2006)

Table 2 continued

Table 2 (*continued*)

HIP Identifier	λ (μm)	F_ν (mJy)	Instrument	References
HIP 95270	170	736.00 ± 192.00	<i>ISO</i>	Moór et al. (2006)
HIP 95270	870	51.70 ± 6.20	APEX/LABOCA	Nilsson et al. (2009)
HIP 95270	1300	7.90 ± 0.20	ALMA	Marino et al. (2016)
HIP 95270	3190	0.72 ± 0.25	ATCA	Lebreton et al. (2012)
HIP 95270	6800	0.14 ± 0.02	ATCA	Ricci et al. (2015b)
HIP 101612	24	204.10 ± 2.05	<i>Spitzer</i> /MIPS	Ballering et al. (2013)
HIP 101612	70	654.00 ± 33.53	<i>Spitzer</i> /MIPS	Ballering et al. (2013)
HIP 101612	70	629.00 ± 44.00	<i>Herschel</i> /PACS	Moór et al. (2015b)
HIP 101612	100	607.00 ± 43.00	<i>Herschel</i> /PACS	Moór et al. (2015b)
HIP 101612	160	405.00 ± 29.00	<i>Herschel</i> /PACS	Moór et al. (2015b)
HIP 101612	250	145.00 ± 14.00	<i>Herschel</i> /SPIRE	Moór et al. (2015b)
HIP 101612	350	70.00 ± 7.00	<i>Herschel</i> /SPIRE	Moór et al. (2015b)
HIP 101612	500	34.00 ± 7.00	<i>Herschel</i> /SPIRE	Moór et al. (2015b)
HIP 101612	870	<21.30	APEX/LABOCA	Nilsson et al. (2010)
HIP 101800	24	76.55 ± 0.77	<i>Spitzer</i> /MIPS	Ballering et al. (2013)
HIP 101800	70	73.32 ± 7.64	<i>Spitzer</i> /MIPS	Ballering et al. (2013)
HIP 106741	24	31.58 ± 0.34	<i>Spitzer</i> /MIPS	Ballering et al. (2013)
HIP 106741	70	217.20 ± 12.98	<i>Spitzer</i> /MIPS	Ballering et al. (2013)
HIP 106741	160	185.60 ± 26.40	<i>Spitzer</i> /MIPS	Moór et al. (2011)
HIP 106741	450	<125.00	JCMT/SCUBA-2	Panić et al. (2013)
HIP 106741	850	5.30 ± 1.40	JCMT/SCUBA-2	Panić et al. (2013)
HIP 114189	24	86.60 ± 0.87	<i>Spitzer</i> /MIPS	Ballering et al. (2013)
HIP 114189	70	610.00 ± 30.95	<i>Spitzer</i> /MIPS	Ballering et al. (2013)
HIP 114189	70	537.00 ± 15.00	<i>Herschel</i> /PACS	Matthews et al. (2014a)
HIP 114189	90	585.00 ± 41.00	<i>ISO</i>	Moór et al. (2006)
HIP 114189	100	687.00 ± 20.00	<i>Herschel</i> /PACS	Matthews et al. (2014a)
HIP 114189	160	555.00 ± 66.00	<i>Spitzer</i> /MIPS	Su et al. (2009)
HIP 114189	160	570.00 ± 50.00	<i>Herschel</i> /PACS	Matthews et al. (2014a)
HIP 114189	250	309.00 ± 30.00	<i>Herschel</i> /SPIRE	Matthews et al. (2014a)
HIP 114189	350	163.00 ± 30.00	<i>Herschel</i> /SPIRE	Matthews et al. (2014a)
HIP 114189	500	<90.00	<i>Herschel</i> /SPIRE	Matthews et al. (2014a)
HIP 114189	850	10.30 ± 1.80	JCMT/SCUBA	Williams & Andrews (2006)
HIP 114189	1340	2.80 ± 0.50	ALMA	Booth et al. (2016)
HIP 117452	24	165.60 ± 1.61	<i>Spitzer</i> /MIPS	Ballering et al. (2013)
HIP 117452	70	54.80 ± 7.16	<i>Spitzer</i> /MIPS	Ballering et al. (2013)
HIP 117452	100	28.89 ± 2.85	<i>Herschel</i> /PACS	Thureau et al. (2014)
HIP 117452	160	<9.70	<i>Herschel</i> /PACS	Thureau et al. (2014)

Table 3. Single-component Fit Results

HIP Identifier	r_{warm} (au)	M_{warm} ($\times 10^{-5} M_{\oplus}$)	f_{warm} ($\times 10^{-5}$)	c_{IRS}
HIP 9902	2.80	0.64	17.00	0.90
HIP 14684	4.40	0.25	5.21	0.92
HIP 17549	10.00	11.02	8.33	0.92
HIP 18217	4.50	0.48	2.65	0.95
HIP 18481	3.30	0.51	3.85	0.99
HIP 23871	7.00	1.55	2.84	0.91
HIP 28103	12.20	0.79	0.82	0.92
HIP 41967	3.30	0.20	5.21	0.95
HIP 49593	5.10	0.50	2.18	0.94
HIP 54879	16.20	4.94	0.98	0.98
HIP 57524	4.50	0.78	9.64	0.92
HIP 57950	6.20	2.10	10.16	0.98
HIP 60348	7.10	2.51	12.24	0.86
HIP 62134	5.60	0.72	4.15	0.92
HIP 63836	3.70	0.60	8.53	0.87
HIP 64053	5.30	3.09	6.03	0.93
HIP 64877	8.10	8.03	20.97	0.93
HIP 67068	2.60	0.23	5.46	0.99
HIP 67230	9.90	19.87	28.98	0.92
HIP 70455	8.10	5.87	5.55	0.97
HIP 74824	7.40	2.35	4.13	0.93
HIP 77315	10.20	22.31	16.16	0.89
HIP 79710	3.80	2.04	19.73	1.00
HIP 79881	8.40	0.75	1.05	0.90
HIP 89770	6.00	3.22	14.85	0.93
HIP 95560	7.20	1.93	3.02	0.93
HIP 106783	10.70	2.19	1.76	0.92
HIP 112542	16.40	12.76	3.21	0.92
HIP 115738	9.10	1.72	1.47	0.91

Table 4. Two-component Fit Results

HIP Identifier	r_{warm} (au)	M_{warm} ($\times 10^{-5} M_{\oplus}$)	f_{warm} ($\times 10^{-5}$)	T_{cold} (K)	f_{cold} ($\times 10^{-5}$)	λ_0	$\tilde{\beta}$	c_{IRS}
HIP 345	8.00	3.07	3.33	56.17	6.09	100.00	1.00	0.96
HIP 682	5.40	0.59	6.18	51.03	35.47	160.00	0.55	0.92
HIP 1473	6.00	0.44	0.99	101.53	0.56	237.43	0.11	0.91
HIP 1481	1.10	0.04	4.91	109.63	4.14	100.00	1.00	0.93
HIP 2472	16.20	3.09	1.02	60.06	0.84	100.00	1.00	0.91
HIP 2710	4.30	0.16	1.84	51.24	11.48	100.00	1.00	0.93
HIP 7805	5.40	0.95	6.42	57.67	29.95	100.00	1.00	0.92
HIP 7978	36.00	16.09	4.23	46.37	24.06	70.00	0.56	0.98
HIP 8241	6.80	1.37	2.10	57.79	7.85	154.25	1.20	0.94
HIP 11360	7.10	1.28	5.34	53.79	45.39	61.15	0.61	0.99
HIP 11477	7.30	0.76	1.44	80.76	3.15	100.00	1.00	0.89
HIP 11847	22.60	160.33	77.27	67.11	120.06	71.42	0.80	0.91
HIP 13141	8.50	0.66	0.90	54.75	4.68	136.05	0.93	0.91
HIP 18859	1.70	0.06	2.76	71.68	7.92	196.02	0.76	0.96
HIP 20901	11.30	2.53	2.08	62.27	3.71	100.00	1.00	0.91
HIP 22192	6.30	0.40	1.32	64.70	3.63	71.42	1.12	0.94
HIP 22226	26.50	37.44	12.21	58.26	74.10	83.52	0.82	0.88
HIP 23451	3.20	5.29	62.92	80.41	482.70	87.34	0.47	0.96
HIP 26453	5.80	1.40	8.31	77.43	24.96	100.00	1.00	0.91
HIP 26796	6.70	3.00	3.39	85.61	3.55	100.00	1.00	0.92
HIP 34276	12.00	1.78	1.13	61.12	25.38	71.42	0.16	1.01
HIP 36948	36.10	67.92	28.64	49.64	203.69	50.00	0.41	0.93
HIP 41152	9.30	1.89	2.63	57.42	6.61	71.42	0.41	0.91
HIP 41373	3.70	0.50	3.05	73.92	8.80	100.77	0.97	0.89
HIP 45167	4.00	1.16	4.69	70.44	4.96	100.00	1.00	0.94
HIP 47135	17.50	3.81	4.32	45.97	16.51	100.00	1.00	0.93
HIP 48423	3.20	0.18	5.68	73.49	7.84	100.00	1.00	0.96
HIP 55485	3.70	0.65	4.23	75.57	2.82	100.00	1.00	0.94
HIP 58720	4.50	2.87	7.19	112.95	7.08	100.00	1.00	0.91
HIP 60074	8.70	1.05	4.74	48.28	93.20	349.97	0.71	1.02
HIP 61684	5.90	4.16	18.42	86.22	34.30	100.00	1.00	0.91
HIP 62657	20.70	125.70	79.60	56.17	135.68	166.66	0.69	0.86
HIP 73145	6.10	22.66	77.36	71.83	240.75	194.79	0.73	1.00
HIP 74499	5.80	2.27	16.80	66.50	83.11	100.00	1.00	0.92
HIP 75077	6.70	1.00	2.01	50.94	4.88	100.00	1.00	1.01
HIP 75210	3.20	1.60	7.62	120.77	3.52	100.00	1.00	0.91
HIP 76736	7.30	4.41	8.96	59.72	41.58	100.00	1.00	0.98
HIP 77432	0.50	0.03	8.68	101.45	13.05	100.00	1.00	0.91
HIP 77464	6.70	0.71	1.67	60.46	7.54	100.00	1.00	0.97
HIP 78043	6.00	2.78	13.70	60.41	62.21	114.20	0.70	1.02
HIP 78045	2.90	0.26	2.25	91.42	2.03	100.00	1.00	0.96
HIP 79516	24.90	295.37	104.69	57.92	205.73	50.53	0.48	0.91
HIP 79742	14.30	37.63	39.87	69.64	182.99	62.45	0.42	0.96
HIP 83187	17.30	5.02	2.25	53.10	5.01	100.00	1.00	0.95
HIP 85537	22.80	10.67	2.25	44.59	5.73	93.26	0.98	0.95
HIP 85922	1.50	0.14	4.11	99.92	1.77	100.00	1.00	0.93
HIP 87108	12.90	5.04	2.72	64.53	7.75	127.18	1.01	0.98
HIP 94114	5.70	0.91	2.12	77.84	0.41	100.00	1.00	0.96

Table 4 continued

Table 4 (*continued*)

HIP Identifier	r_{warm} (au)	M_{warm} ($\times 10^{-5} M_{\oplus}$)	f_{warm} ($\times 10^{-5}$)	T_{cold} (K)	f_{cold} ($\times 10^{-5}$)	λ_0	$\tilde{\beta}$	c_{IRS}
HIP 95270	33.80	324.22	72.14	60.43	215.48	55.16	0.50	1.00
HIP 101612	17.10	2.57	1.38	43.90	7.87	71.42	0.96	0.89
HIP 101800	12.90	3.36	2.03	61.59	1.58	100.00	1.00	0.92
HIP 106741	8.00	0.59	2.09	52.27	33.65	152.58	0.62	0.96
HIP 114189	3.90	0.46	4.36	44.51	29.16	200.82	1.18	1.09
HIP 117452	3.30	0.32	1.68	130.00	0.88	100.00	1.00	0.94